

Multi-vortex Bose-Einstein Condensate: role of interaction-range

Md Hamid^{1,*} and M. A. H. Ahsan^{1,†}

¹*Department of Physics, Jamia Millia Islamia (A Central University), New Delhi 110025, India.*

(Dated: November 1, 2023)

Abstract

We present an exact diagonalization study on a system of $10 \leq N \leq 24$ spinless bosons interacting via a repulsive Gaussian potential, harmonically confined in x - y plane with an externally impressed rotation about the z -axis. The diagonalization of the N -body Hamiltonian matrix, in subspaces of total angular momentum in the regime $0 \leq L_z \leq 4N$, is carried out to obtain the variationally exact ground-state wavefunction. The one-particle reduced density matrix(OPRDM) is obtained in beyond Lowest-Landau Level as well as Lowest-Landau Level approximation. The two-body interaction strength g_2 in the Gaussian potential is taken in the strongly interacting regime with varying values of interaction range σ . An increase in interaction range σ leads to an increase in (a) the occupation of the maximally occupied one-particle state (b) the largest eigenvalue λ_1 (condensate fraction) of OPRDM and (c) the critical angular velocity Ω_{c_i} of the i th vortical state. To quantify the quantum entanglement between the particles in the many-body ground state, we calculate the von Neumann entropy $S_1(L_z, \sigma)$ which is largely found to decrease with increase in interaction range σ . Crossings in von Neumann entropy $S_1(L_z, \sigma)$ for several of the angular momentum states are observed with variation in σ . The response of the Bose-Einstein Condensate to rotation is examined through $L_z(\sigma) - \Omega(\sigma)$ stability graph for various values of σ . A vortex state with larger span (plateau) on the $L_z - \Omega$ graph is found to be more stable. Consequently, the two-vortex state is less stable compared to the single-vortex and the three-vortex states. The internal structure of the condensate, as depicted by the conditional probability distribution(CPD) in the body-fixed frame, is found to change with interaction range. One such effect is the merging of the cores of the two-vortex state as interaction range σ is increased beyond a critical value.

* hamidjmi2008@gmail.com

† mahsan@jmi.ac.in

I. INTRODUCTION

Advancements in cooling, trapping and manipulation of atoms achieved over decades of intensive research[1–5] have led to creation of ultracold dilute atomic vapours with tunable parameters in laboratories. This has opened up the possibility of investigating quantum many-body effects in a controlled environment. Vapours of weakly interacting alkali atoms such as ^{23}Na , ^{39}K , ^{87}Rb , with repulsive [6–8], and ^7Li , with attractive interaction [9, 10] confined in a magnetic trap and cooled to nanokelvin temperatures have been created in laboratories. One of the landmark achievements has been the realization of Bose-Einstein condensation(BEC) in trapped atomic Bose gases [6, 7, 9]. Dilute fermionic gas of ^{40}K atoms at very low temperatures have also been studied [11, 12]. An interesting phenomena studied in dilute atomic gases is the crossover between Bose-Einstein condensation (BEC) and Bardeen-Cooper-Schrieffer (BCS) superfluidity [13, 14]. It involves gradual transition between a gas of weakly interacting bosonic particles (BEC regime) and a gas of weakly interacting fermionic pairs (BCS regime) wherein interatomic interactions are varied from repulsive to attractive using techniques like Feshbach resonances [5].

A fundamental characteristic of Bose-Einstein condensate is its response to rotation that leads to nucleation of quantized vortices[15]. Quantized vortices have been observed in superfluid ^4He as stable topological objects [16]. In type-II superconductors, quantized vortices arrange themselves in regular triangular lattice pattern which leads to the formation of Abrikosov lattice [17]. Madison *et.al.* [18] stirred a cloud of ^{87}Rb atoms using focused laser beam which led to the experimental realization of quantized vortices in Bose-condensed atomic gases [19–24]. The rotating condensate with quantized vortices comprises both of the phase-coherent superfluid quasiparticles carrying quantized angular momenta and the uncondensed non-rotating components residing in the cores of the vortices. On further increasing

the angular velocity Ω , the condensate depletes and an increasing number of particles occupy the cores of vortices. When the number of vortices become large, it becomes convenient to introduce the filling fraction $\nu = N/N_v$, defined as the ratio of the number of bosons N to the average number of vortices N_v . The filling fraction ν is a controlling parameter for vortex-lattice to vortex-liquid quantum phase transition at zero temperature [21, 25]. On the basis of the exact diagonalization studies with periodic boundary conditions on a quasi-2D system, it has been suggested that the vortex-lattice melts [21, 26] due to quantum fluctuations when the filling fraction is of order $\nu \sim 6$ [21].

The short-range inter-atomic interaction in dilute atomic vapours has theoretically been analysed in terms of the singular δ -function potential [27–29] with a single parameter a_s , the s -wave scattering length. The sign of a_s is positive for repulsive interaction [30–33] and negative for attractive interaction [9]. In our present study, we employ finite-range Gaussian potential [27, 29, 34–43] which, unlike δ -function potential which is singular, is smooth and provides control over the inter-atomic interaction through variation of two parameters, namely, the strength of the interaction as measured by the s -wave scattering length a_s and the range of the interaction as measured by the width σ of the Gaussian potential.

The inter-particle interaction gives rise to phase rigidity to the ground-state many-body wavefunction responsible for superfluid flow. The superflow manifests itself in successive appearance of vortices with quantized circulations [35] at critical angular velocities Ω_{c_i} , $i = 1, 2, \dots$, in response to externally impressed rotation. Quantized vortices have been extensively studied since the first observation of BEC in atomic gases [6, 7, 9, 44, 45]. In our present Exact Diagonalization(ED) study on $N = 10, 12, 16$ spinless bosons in the beyond Lowest-Landau Level(LL) approximation and $N = 20, 24$ spinless bosons in the Lowest-Landau Level approximation, we observe that for $L_z = 2N$ state, the vortex cores merge with increase in the range of

interaction in the Gaussian interaction potential.

A useful quantity to theoretically investigate the criterion of symmetry-breaking in a quantum many-body system of bosons is the one-particle reduced density matrix OPRDM $\rho^{(1)}(\mathbf{r}, \mathbf{r}') = \sum_{\mu} \lambda_{\mu} \chi_{\mu; m^{\mu}}(\mathbf{r}) \chi_{\mu; m^{\mu}}(\mathbf{r}')$, comprising of several symmetry-broken states (fractions) labelled by one-particle angular momentum quantum number m^{μ} for the μ -th broken state (fraction) weighted by the corresponding eigenvalue λ_{μ} of OPRDM. Further, at $\mathbf{r} = \mathbf{r}'$, OPRDM reduces to one-particle density *i.e.* $\rho^{(1)}(\mathbf{r}, \mathbf{r}) = n(\mathbf{r})$. For a quasi-2D system, this one-particle density presents cylindrically symmetric distribution [35, 46] with $n(r) = n(r_{\perp})$. Another physical quantity of interest that can be obtained from OPRDM is the von Neumann entropy which is a measure of quantum entanglement in the many-body system [47–52].

Conditional probability distribution(CPD) is an important quantity to study the internal structure of quantum many-body systems like Bose-Einstein Condensate [41, 46, 59], quantum dots, Wigner molecules [54], doubly excited helium-like atoms [55, 56] etc. To examine the internal structure of the ground state of the Bose-Einstein Condensate with total angular momentum L_z , as seen in the body-fixed frame, the CPD is obtained from the many-body ground state wavefunction.

We observe that with increase in interaction range σ , the largest condensate fraction λ_1 of OPRDM increases as shown in Table. V. This may be the consequence of the quantum mechanical phase coherence spreading over more number of particles with increase in σ . For the non-rotating $L_z = 0$ state, most of the particles are distributed around the centre of the trap $(0, 0)$ due to the Gaussian density-profile $n_0(\mathbf{r}) \sim e^{-\alpha_{\perp}^2 r_{\perp}^2}$. For a given interaction strength g_2 , as the number of particles N increases, the effective particle-particle interaction $\approx g_2(N - 1)n_0(\mathbf{r})$ in the mean-field approximation, increases leading to the depletion of the condensate fraction λ_1 . On the other hand, for the single-vortex state, the particles are spread out due to centrifugal

gal force with density profile $n_1(\mathbf{r}) \sim (\alpha_\perp r_\perp)^2 e^{-\alpha_\perp^2 r_\perp^2}$, which vanishes at the centre of the trap (0,0). Thus, the effective particle-particle interaction $\approx g_2(N-1)n_1(\mathbf{r})$ in the mean-field approximation, decreases which leads to increase in the condensate fraction λ_1 for the single-vortex state.

This paper is organised as follows: In Sec. II, we describe the Hamiltonian for harmonically trapped spinless bosons interacting via a Gaussian potential. Sec. III presents brief descriptions of the quantities of interest like the critical angular velocity Ω_c , one particle reduced density matrix(OPRDM), von Neumann entropy S_1 and the conditional probability distribution(CPD) along with our results. In Sec. IV, we present the summary and conclusion of our study. Finally in Appendix, we obtain expressions for (a) one-particle density, (b) conditional probability distribution(CPD) and (c) asymmetry in Hamiltonian to set the condensate in rotation, in the beyond Lowest Landau Level approximation and compare them with Eq.(9), Eq.(14) and Eq.(17), respectively, in reference [46] in the Lowest Landau Level approximation.

II. THE SYSTEM AND THE HAMILTONIAN

We consider a harmonically trapped system of N spinless bosons each of mass M , interacting via a normalized Gaussian potential in an x - y symmetric plane with an externally impressed rotation $\mathbf{\Omega} = \Omega \hat{z}$ about the z -axis. The Hamiltonian for this system in a co-rotating frame is given by

$$\mathbf{H}^{rot} = \mathbf{H}^{lab} - \Omega L_z^{lab}, \quad (1)$$

where $L_z^{lab} = \sum_i^N l_{z_i}$ is the total angular momentum of the system about z -axis in the laboratory frame. The Hamiltonian in the laboratory frame is given by

$$\mathbf{H}^{lab} = \sum_{i=1}^N \left[\frac{\mathbf{P}_i^2}{2M} + V(\mathbf{r}_i) \right] + \sum_{i<j} U(\mathbf{r}_i, \mathbf{r}_j). \quad (2)$$

The first and the second term in Eq. (2) are the kinetic energy and the harmonic trap potential respectively. The last term $U(\{\mathbf{r}, \mathbf{r}'\})$ is the particle-particle interaction potential taken here as a finite-range Gaussian potential described ahead. The harmonic potential can be written as

$$V(\mathbf{r}) = \frac{1}{2}M(\omega_{\perp}^2 r_{\perp}^2 + \omega_z^2 z^2) = \frac{1}{2}M\omega_{\perp}^2 (r_{\perp}^2 + \lambda_z^2 z^2), \quad (3)$$

where $r_{\perp} = \sqrt{x^2 + y^2}$ is the radial distance from the axis of rotation and ω_{\perp} , ω_z are the radial and axial trap frequencies respectively with the anisotropy parameter (aspect ratio) $\lambda_z \equiv \omega_z/\omega_{\perp}$. We assume our system to be highly oblate spheroidal with $\lambda_z \gg 1$ [57, 58]. In terms of these trap frequencies and the mass of the particle, we can write the harmonic oscillator lengths *i.e.* the radial length $a_{\perp} = \sqrt{\frac{\hbar}{M\omega_{\perp}}}$ and the axial length $a_z = \sqrt{\frac{\hbar}{M\omega_z}}$.

The particle-particle Gaussian interaction potential [27, 34–37] is given by

$$U(\mathbf{r}, \mathbf{r}') = g_2 \left(\frac{1}{\sqrt{2\pi}\sigma} \right)^2 \exp \left[-\frac{(r_{\perp} - r'_{\perp})^2}{2\sigma^2} \right]. \quad (4)$$

Here, the interaction strength is given by $g_2 = \frac{4\pi a_s}{a_{\perp}}$ where a_s is the s-wave scattering length and σ is the particle-particle interaction range scaled by a_{\perp} .

In experiments, focused laser beam is used to stir a Bose-Einstein condensate confined in a magnetic trap which leads to the creation of vortices beyond a critical velocity [18, 75]. Theoretically, this is achieved by introducing a small perturbative potential [46] with A as the small dimensionless parameter:

$$\begin{aligned} V_p &= \frac{A}{2}M\omega_{\perp}^2 \sum_{i=1}^N (x_i^2 - y_i^2) \\ &= \frac{A}{2}M\omega_{\perp}^2 \sum_{i=1}^N r_{\perp i}^2 \cos(2\phi_i) \end{aligned} \quad (5)$$

which breaks the azimuthal symmetry in the x - y plane. The full Hamiltonian now becomes $\mathbf{H} = \mathbf{H}^{lab} + Vp$. We assume $A/[2\hbar(\omega_{\perp} - \Omega)] \ll 1$ is small and thus ignore the perturbative term in the results presented in our study here. The exact diagonalization of the Hamiltonian is performed in subspaces of total angular momentum L_z . Further discussion on the perturbative term V_p in beyond Lowest Landau Level approximation is presented in Appendix C.

III. RESULTS AND DISCUSSIONS

We present in our study results for the ground-state of $N = 10, 12, 16$ spinless bosons, at zero temperature, in the beyond lowest Landau level approximation and for $N = 20, 24$ in the lowest Landau level approximation. The values of anisotropy parameter (aspect ratio) and the confining frequency are taken as $\lambda_z = \sqrt{8}$ and $\omega_{\perp} = 2\pi \times 220$ Hz respectively [57, 58]. Due to large aspect ratio, there will practically be no excitation along the z -axis. The parameters have been chosen corresponding to ^{87}Rb atom [57] for which the trap length turns out to be $a_{\perp} = \sqrt{\hbar/(M\omega_{\perp})} = 0.727\mu\text{m}$ and the s-wave scattering length $a_s = 100a_0$, where a_0 is the Bohr radius. The dimensionless parameter for particle-particle interaction strength for a system of N bosons is proportional to Na_s/a_{\perp} . As the number of particles N increases, the dimensionality of the many-particle Hilbert space increases exponentially. Since we have limited computational resources to increase the number of particles N , we increase the scattering length to $a_s = 1000a_0$ to get the value of the parameter Na_s/a_{\perp} closer to experimental situation [57] with $g_2 = 0.9151$ for $N = 10$ to 24. The rotation Ω is considered in slowly to rapidly rotating regime with angular momenta $0 \leq L_z \leq 4N$ to study its effects on quantum mechanical properties of the condensate viz. the critical angular velocity, condensate fraction, nucleation of vortices and merging of the cores of vortices. In the quasi-2D x - y plane,

the inter-particle spacing is proportional to $\frac{a_{\perp}}{\sqrt{N}}$ which for $N = 16$ becomes $0.25a_{\perp}$. For a given interaction strength g_2 , the interaction range σ is varied from 0.1 to 1.0 (in units of a_{\perp}) in the Gaussian potential in Eq. (4), to examine the role of σ in quantum many-body effects. In particular, we have considered $\sigma = 0.3, 0.5$ and 0.75 (in units of a_{\perp}).

Most of the theoretical work reported in the literature have focused on the Lowest Landau-Level (LLL) approximation, in which one takes the one-particle basis states in Eq. (9) with radial quantum $n_r = 0$, while the one-particle angular momentum quantum number m takes positive values only. This reduces the dimensionality of the Hilbert space significantly [59, 60]. In moderately to strongly interacting and slowly rotating regime [35], the beyond-LLL approximation is considered a better approximation over LLL approximation [36, 37, 39] with $n_r = 0, 1, 2, \dots$ while m is allowed to take both positive and negative ($\pm m$) values. For computational feasibility, it is necessary to select a finite number of one-particle basis states to construct the many-particle basis states for determination [35–37] of the variationally exact ground state wavefunction $\Psi_0(\mathbf{r}_1, \mathbf{r}_2, \dots, \mathbf{r}_N)$ given by the eigenvalue equation:

$$\begin{aligned} \mathbf{H}^{lab} \Psi_0(\mathbf{r}_1, \mathbf{r}_2, \dots, \mathbf{r}_N) = & E_0^{lab}(L_z, g_2, \sigma) \\ & \Psi_0(\mathbf{r}_1, \mathbf{r}_2, \dots, \mathbf{r}_N) \end{aligned} \quad (6)$$

where \mathbf{H}^{lab} is the many-body Hamiltonian in Eq. (1) and $E_0^{lab}(L_z, g_2, \sigma)$ the corresponding interacting ground state energy in the laboratory frame for a given number of bosons N and in given subspaces of the total angular momentum L_z .

A. Critical angular velocity

When the condensate is subjected to an externally impressed rotation with angular velocity Ω , the non-zero angular momentum states $\{L_z^i \neq 0, (i = 1, 2, 3, \dots)\}$

successively become the ground state in the corotating frame at the corresponding critical angular velocities $\{\Omega_{c_i}, (i = 1, 2, 3, \dots)\}$ by [35–37]

$$\Omega_{c_i}(L_z^i, g_2, \sigma) = \frac{E_0^{lab}(L_z^i, g_2, \sigma) - E_0^{lab}(L_z^{(i-1)}, g_2, \sigma)}{L_z^i - L_z^{(i-1)}}, \quad (7)$$

where $E_0^{lab}(L_z^i, g_2, \sigma)$ is the ground state energy in the laboratory frame given by Eq. (6) for the i^{th} vortical state with angular momentum $L_z^i(\Omega)$.

To analyse the response of the condensate to rotation, we plot $L_z - \Omega$ stability graph as in Fig. 1 for various values of interaction range σ . We observe that the angular momentum $L_z = 0$ state remains the ground state of the system till the angular velocity attains the first critical value Ω_{c_1} . As the system is subjected to further rotation, higher angular momentum states with $L_z > 0$, which minimize the Helmholtz free energy at zero temperature $F = \langle \Psi_0 | (\mathbf{H}^{lab} - \hbar\Omega L_z) | \Psi_0 \rangle$ in the co-rotating frame, become the successive ground states of the system at a series of critical angular velocities $\{\Omega_{c_i}, i = 1, 2, \dots\}$. Each of ground state corresponding to $\Omega_{c_i}(L_z^i, g_2, \sigma)$ is referred to as the i^{th} stable, phase-coherent vortical state [61, 62]. The horizontal plateaus on the $L_z - \Omega$ stability graph in Fig. 1 represent the span of the stable angular momentum state L_z^i and the vertical step show the quantum jump in angular momentum L_z at the corresponding critical angular velocity Ω_{c_i} .

We also observe from Table I that for given values of parameters, the value of respective critical angular velocity of the i^{th} vortical state increases for increasing values of the interaction range σ in slowly to moderately rotating regime *i.e.* $\Omega_{c_i}(\sigma') > \Omega_{c_i}(\sigma)$ for $\sigma' > \sigma$. For example, for the non-rotating $L_z = 0$ state, the first critical angular velocity for various values of σ are: $\Omega_{c_1}(\sigma = 0.30) = 0.774$, $\Omega_{c_1}(\sigma = 0.50) = 0.784$ and $\Omega_{c_1}(\sigma = 0.75) = 0.818$. Thus an increase in interaction range σ results in an enhanced stability of the i^{th} vortical state with total angular momen-

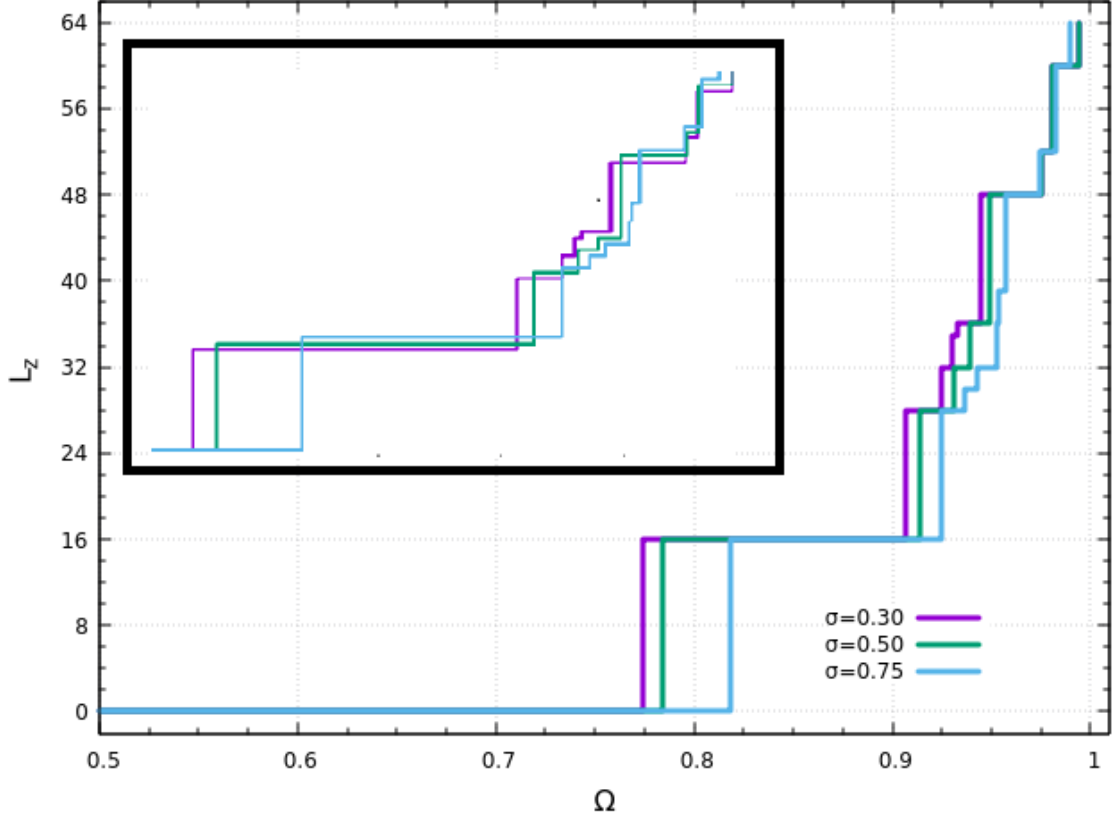


FIG. 1. (Color online) The $L_z - \Omega$ stability graph for $N = 16$ with interaction strength $g_2 = 0.9151$ and three values of interaction range $\sigma = 0.30, 0.50, 0.75$. For each value of σ , a set of critical angular velocities $\{\Omega_{c_i}(\sigma), i = 1, 2, 3, \dots\}$ is observed where the total angular momentum L_z takes a quantum jump. (In the inset, values on y-axis has been shifted upward for better view.)

tum $L_z^i(\Omega_{c_i})$ leading to delayed onset of the next vortical state $L_z^{i+1}(\Omega_{c_{i+1}})$ i.e. $\Omega_{c_{i+1}}(\sigma') > \Omega_{c_{i+1}}(\sigma)$ for $\sigma' > \sigma$. However, the span of the plateau on the $L_z - \Omega$ stability graph for a given vortical state L_z^i decreases with increase in σ i.e. $(\Omega_{c_{i+1}}(\sigma') - \Omega_{c_i}(\sigma')) < (\Omega_{c_{i+1}}(\sigma) - \Omega_{c_i}(\sigma))$ for $\sigma' > \sigma$. For example, for the stable

angular momentum state $L_z = 16$, the spans on the $L_z - \Omega$ stability graph for various values of σ are: $\Omega_{c_2}(0.30) - \Omega_{c_1}(0.30) = 0.1325$, $\Omega_{c_2}(0.50) - \Omega_{c_1}(0.50) = 0.12957$ and $\Omega_{c_2}(0.75) - \Omega_{c_1}(0.75) = 0.10627$. One observes a series of quantum jumps in angular momentum $\{L_z^i(\Omega_{c_i}), i = 1, 2, 3, \dots\}$ on the $L_z - \Omega$ stability graph and the corresponding plateaus for different interaction range σ are given in bold in Table IV. For example, for the single vortex state $L_z = N = 16$, the jump to the next stable angular momentum state $L_z = 28$ for various values of σ are: $\Omega_{c_2}(\sigma = 0.30) = 0.907$, $\Omega_{c_2}(\sigma = 0.50) = 0.914$ and $\Omega_{c_2}(\sigma = 0.75) = 0.925$. An increase in interaction range σ leads to an increase in the value of critical angular velocity Ω_{c_i} of the i th vortical state as opposed to decrease in the value of critical angular velocity Ω_{c_i} with increase in interaction strength g_2 and the number of particles. [35, 53].

We also observe that with increase in interaction range σ , some new plateaus appear on the $L_z - \Omega$ stability graph in Fig. 1. For example for $\sigma = 0.75$, an additional stable plateau appears at $L_z = 30$, which is not observed for $\sigma = 0.30, 0.50$. Similarly for $\sigma = 0.75$, an additional stable plateau appears at $L_z = 39$. Thus the underlying symmetry of the quantum many-body state is further broken with increase in σ beyond a critical value.

We observe from the Table. II that, for $N = 16$ with $g_2 = 0.9151$ and $\sigma = 0.30$, the non-rotating angular momentum $L_z = 0$ state remains the ground state of the system till $L_z(\Omega_{c_1}) = N$. Hence the $L_z = 0$ state remains the (stable) ground state over a span of $L_z(\Omega_{c_1}) - L_z(\Omega = 0) = 16$ units of angular momentum. The single-vortex state nucleates at $L_z = N = 16$ and remains the ground state till $L_z = 28$ with a span of $L_z(\Omega_{c_2}) - L_z(\Omega_{c_1}) = 12$ units of angular momentum. The two-vortex state remains the ground state of the system till $L_z = 36$ with a span of $L_z(\Omega_{c_3}) - L_z(\Omega_{c_2}) = 8$ units of angular momentum. Thus the three-vortex state nucleates readily from the two-vortex state with just 8 units of angular momentum.

The three-vortex state nucleates at $L_z = 36$ and remains the ground state of the system till $L_z = 48$ with a span of $L_z(\Omega_{c_4}) - L_z(\Omega_{c_3}) = 12$ units of angular momentum. The four-vortex state nucleates at $L_z = 48$ and remains the ground state of the system till $L_z = 60$ with a span of $L_z(\Omega_{c_5}) - L_z(\Omega_{c_4}) = 12$ units of angular momentum. It is apparent from the Table. II that among the multi-vortex states, the two-vortex, the four-vortex, the five-vortex states requires more units of angular momentum to nucleate. The three-vortex state with triangular geometry nucleates readily from the two-vortex state with just 8 units of angular momentum and remains the ground state over a span of 12 units of angular momentum before the four-vortex state nucleates. The single-vortex state is more stable than the multi-vortex states. Among the multi-vortex states, the three-vortex state is more stable in comparison to the two-vortex state with diagonally placed vortices with respect to the centre of the trap. This finding supports the experimental analysis found in literature [18].

B. The one-particle reduced density matrix: beyond LLL approximation

The one particle reduced density matrix (OPRDM) provides a criterion for Bose-Einstein condensation [63, 64, 66–68] in a system of bosons at small but finite temperature. It provides information about one-body observables for a many-body system.

Having obtained the variationally exact N -body ground state wave-function $\Psi_0(\mathbf{r}_1, \mathbf{r}_2, \dots, \mathbf{r}_N)$ from Eq. (6), the OPRDM $\rho^{(1)}(\mathbf{r}, \mathbf{r}')$ is found [35] by tracing

out the degrees of freedom corresponding to $(N - 1)$ particles:

$$\begin{aligned}
\rho^{(1)}(\mathbf{r}, \mathbf{r}') &\equiv \int \int \cdots \int d\mathbf{r}_2 d\mathbf{r}_3 \cdots d\mathbf{r}_N \\
&\times \Psi_0(\mathbf{r}, \mathbf{r}_2, \mathbf{r}_3 \cdots, \mathbf{r}_N) \Psi_0^*(\mathbf{r}', \mathbf{r}_2, \mathbf{r}_3 \cdots, \mathbf{r}_N) \\
&= \sum_{n_r} \sum_m \sum_{n'_r} \sum_{m'} \rho_{n_r, m; n'_r, m'} \\
&\times u_{n_r, m}(\mathbf{r}) u_{n'_r, m'}^*(\mathbf{r}')
\end{aligned}$$

where $u_{n_r, m}(\mathbf{r})$ is the one-particle harmonic oscillator basis state in 2-dimension given by

$$\begin{aligned}
u_{n_r, m}(r_\perp, \phi) &= \sqrt{\frac{\alpha_\perp^2 n_r!}{\pi(n_r + |m|)!}} e^{im\phi} (r_\perp \alpha_\perp)^{|m|} \\
&\times e^{-\frac{1}{2}\alpha_\perp^2 r_\perp^2} L_{n_r}^{|m|}(r_\perp^2 \alpha_\perp^2).
\end{aligned} \tag{8}$$

$$n_r = 0, 1, 2, \cdots \quad \text{and} \quad m = 0, \pm 1, \pm 2, \cdots$$

Here $L_{n_r}^{|m|}(r_\perp^2 \alpha_\perp^2)$ is the associated Laguerre polynomial, n_r the radial quantum number and m the angular momentum quantum number. The OPRDM $\rho^{(1)}(\mathbf{r}, \mathbf{r}')$, can be diagonalized to give

$$\rho^{(1)}(\mathbf{r}, \mathbf{r}') = \sum_{\mu=1}^{\mathcal{M}} \lambda_\mu \chi_{\mu; m^\mu}(\mathbf{r}) \chi_{\mu; m^\mu}^*(\mathbf{r}') \tag{9}$$

$$\text{with } \hat{l}_z \chi_{\mu, m^\mu} = m^\mu \chi_{\mu, m^\mu} \tag{10}$$

$$\text{and } \chi_{\mu, m^\mu}(\mathbf{r}) = \sum_{n_r^\mu=0,1,2,\dots} c_{n_r^\mu, m^\mu} u_{n_r^\mu, m^\mu}(\mathbf{r}) \tag{11}$$

where $\{\lambda_\mu\}$ are the eigenvalues of OPRDM, $\{\chi_{\mu; m^\mu}\}$ are the corresponding simultaneous eigenvectors of OPRDM and one-particle angular momentum \hat{l}_z . The various eigenvalues $\{\lambda_\mu\}$ of OPRDM give the fraction of the corresponding one-particle symmetry-broken eigenstates $\{\chi_{\mu; m^\mu}\}$ of OPRDM labelled by μ and the one-particle

angular momentum quantum number m^μ . The eigenvectors of OPRDM are normalized and eigenvalues satisfy the following sum rule

$$\sum_{\mu=1}^{\mathcal{M}} \lambda_\mu = 1 \text{ and } \sum_{\mu=1}^{\mathcal{M}} m^\mu \lambda_\mu = L_z/N. \quad (12)$$

For a system comprising of a finite number of particles, the criterion for Bose-Einstein condensation is that one or a few of the eigenvalues $\{\lambda_\mu\}$ of OPRDM become significantly large compared to others [64, 66, 68].

As the number of particles in the condensate becomes large *i.e.* $\Delta N \rightarrow \infty$, it follows from the commutation relation between the number operator and the quantum mechanical phase operator $[\hat{N}, \hat{\Theta}] = \hbar$ that the fluctuation in the phase of the condensate vanishes *i.e.* $\Delta\Theta \rightarrow 0$ and the system acquires a definite quantum mechanical phase leading to a situation where $\lambda_1 \sim 1$ and $\lambda_2 \approx \lambda_3 \approx \dots \approx 0$. For a system comprising of finite number of particles *i.e.* $\Delta N \rightarrow$ finite, the quantum mechanical phase of the condensate fluctuates over the phases of symmetry-broken eigenstates $\{\chi_{\mu;m^\mu}\}$ of OPRDM [65, 68]. Thus the OPRDM defined in Eq. (9) is the quantum mechanical average with weights $\{\lambda_\mu\}$ over the symmetry-broken [65] eigenstate states $\{\chi_{\mu;m^\mu}\}$ with definite one-particle angular momentum quantum number m^μ , where $\mu = 1, 2, \dots, \mathcal{M}$ are different fragments of the OPRDM. This may cause more than one eigenvalues of OPRDM to take significantly large values as compared to others and may lead to the fragmentation of the rotating condensate comprising of a finite number of particles. Further, the fragmentation of the condensate, as described by OPRDM, is an interplay of parameters like the interaction strength g_2 , the interaction range σ , the angular momentum $L_z(\Omega)$ and the number of particles N .

In Fig. 2, we observe that the largest condensate fraction λ_1 is maximum for the non-rotating state $L_z = 0$ and decreases with increasing total angular momentum L_z . However, the second largest condensate fraction λ_2 which is minimum for the non-

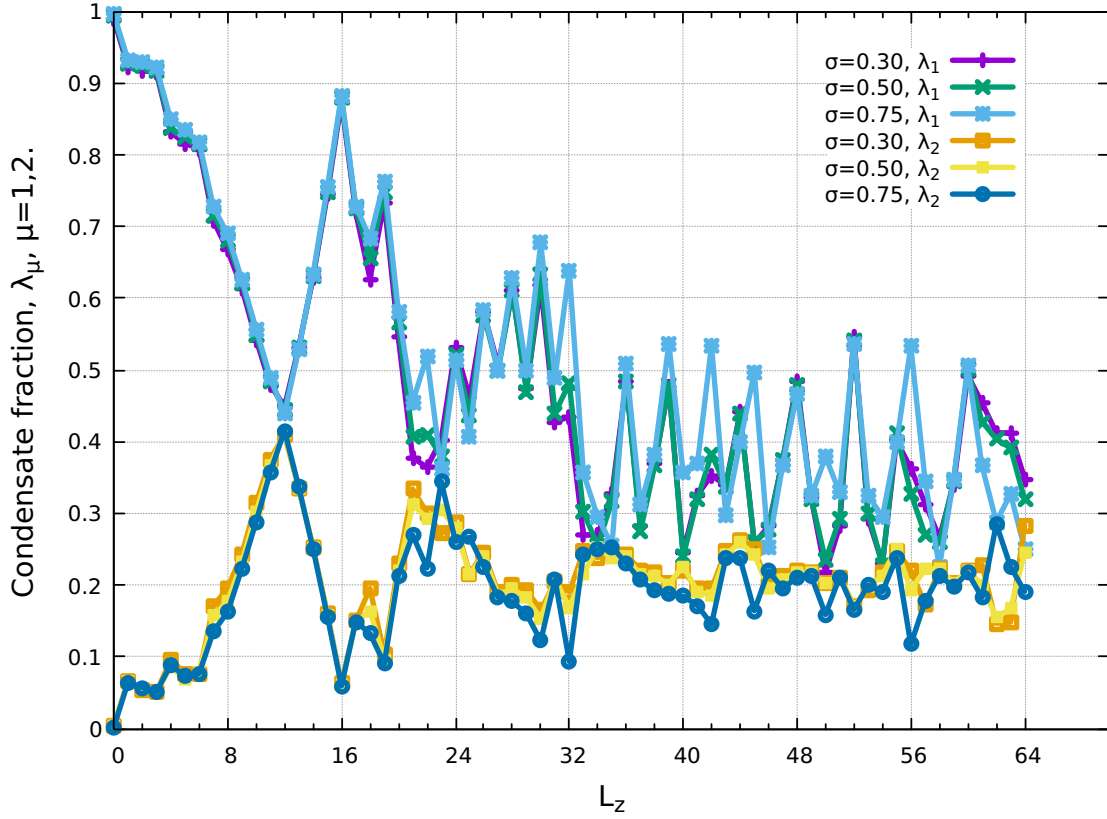


FIG. 2. (Color online) Two of the largest condensate fractions $\lambda_1 > \lambda_2$ vs the total angular momentum L_z in the regime $0 \leq L_z \leq 4N$ for $N = 16$ bosons with interaction strength $g_2 = 0.9151$ and three values of interaction range $\sigma = 0.30, 0.50, 0.75$.

rotating state, increases with increasing L_z and becomes comparable *i.e.* $\lambda_2 \approx \lambda_1$ for different values of interaction range σ at total angular momentum L_z as given in Table III.

C. von Neumann entropy

In order to examine the quantum entanglement between the particles in the ground state of the condensate, we calculate the von Neumann entropy defined in terms of OPRDM $\hat{\rho}^{(1)}$ as follows [49, 69–71],

$$S_1 = -\text{Tr} (\hat{\rho}^{(1)} \ln \hat{\rho}^{(1)}) = -\sum_{\mu=1}^{\mathcal{M}} \lambda_{\mu} \ln \lambda_{\mu} \quad (13)$$

where μ labels the symmetry-broken one-particle eigenstates of OPRDM.

We observe from Fig. 3 that the non-rotating $L_z = 0$ condensate for $N = 16$ bosons has the lowest value of von Neumann entropy for all the three values of interaction range $\sigma = 0.30, 0.50, 0.75$ considered here. It is further observed that with increase in angular momentum, the von Neumann entropy $S_1(L_z, \sigma)$ increases upto $L_z = 11$ and then it decreases taking minimum value for the single-vortex $L_z = N = 16$ state. It is also observed that in the slowly rotating regime $0 < L_z \leq N$, the von Neumann entropy $S_1(L_z, \sigma)$ overlaps for different values of interaction range σ . However, in the moderately rotating regime $N < L_z \leq 2N$, the von Neumann entropy $S_1(L_z, \sigma)$ is non-overlapping for different values of σ . In the rapidly rotating regime $L_z > 2N$, there is significant variations in $S_1(L_z, \sigma)$ for different values of σ . For a given total angular momentum L_z state, the von Neumann entropy $S_1(L_z, \sigma)$ is lower for higher values of interaction range σ *i.e.* $S_1(L_z, \sigma') < S_1(L_z, \sigma)$ for $\sigma' > \sigma$ [36].

In Table IV, we list the angular momentum L_z states for which S_1 has a local minima, for three values of interaction range $\sigma = 0.30, 0.50, 0.75$. The angular momentum states in bold-face are the stable states and others are the meta-stable states. The angular momentum states $L_z = 30, 39$ which are meta-stable states at interaction range $\sigma = 0.30, 0.50$, as seen in the $L_z - \Omega$ stability graph in Fig. 1 and Table. IV, become stable states with increase in interaction range to $\sigma = 0.75$

In Fig. 4, we present variation in the von Neumann entropy $S_1(L_z, \sigma)$ with interac-

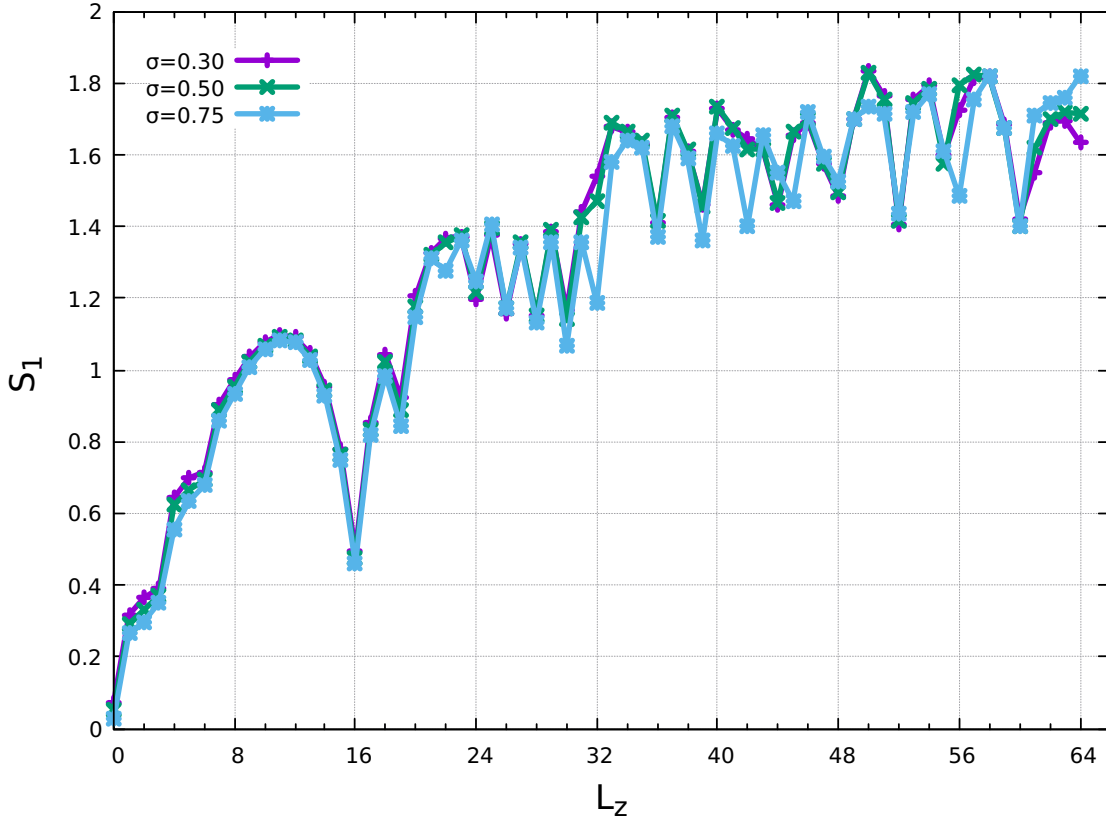


FIG. 3. (Color online) The von Neumann entropy $S_1(L_z, \sigma)$ vs the total angular momentum in the regime $0 \leq L_z \leq 4N$ for $N = 16$ bosons with interaction strength $g_2 = 0.9151$ and three values of interaction range $\sigma = 0.30, 0.50, 0.75$. Decrease in the value of von Neumann entropy S_1 is observed with an increase in the interaction range *i.e.* $S_1(\sigma') < S_1(\sigma)$ for $\sigma' > \sigma$.

tion range $0 \leq \sigma \leq 1$ for certain angular momentum L_z states listed in Table IV. For values of σ in the regime $0 \leq \sigma \leq 1$, the single-vortex states $L_z = N = 16$ have minimum values of $S_1(L_z, \sigma)$ among all the angular momentum $L_z = 16, 28, 30, 32, 36, 39$ states, *i.e.* it is the maximally entangled state well isolated from other angular mo-

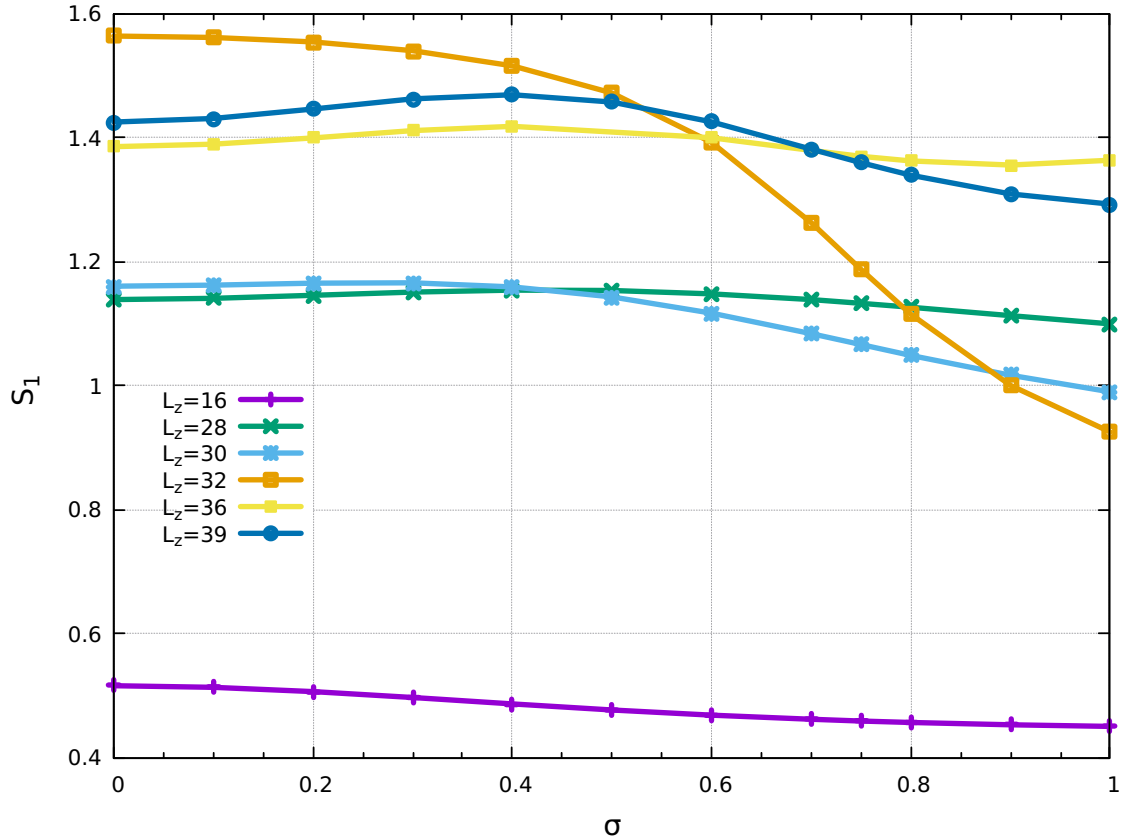


FIG. 4. (Color online) The von Neumann entropy $S_1(L_z, \sigma)$ vs the interaction range in the regime $0 \leq \sigma \leq 1$ with interaction strength $g_2 = 0.9151$, for $N = 16$ bosons for some of the total angular momentum states, namely, $L_z = 16, 28, 30, 32, 36, 39$, listed in Table IV. We observe several crossings in the von Neumann entropy $S_1(L_z, \sigma)$ of different angular momentum states as the interaction range is varied over $0 \leq \sigma \leq 1$.

mentum states listed in Table IV. We further observe that there are crossings in the von Neumann entropy $S_1(L_z, \sigma)$ for $0 \leq \sigma \leq 1$ as seen in Fig. 4. Among the angular momentum states $L_z = 28, 30, 32, 36, 39$, we observe that for the angular momentum $L_z = 32$ state, the von Neumann entropy $S_1(L_z, \sigma)$ is maximum at $\sigma = 0$,

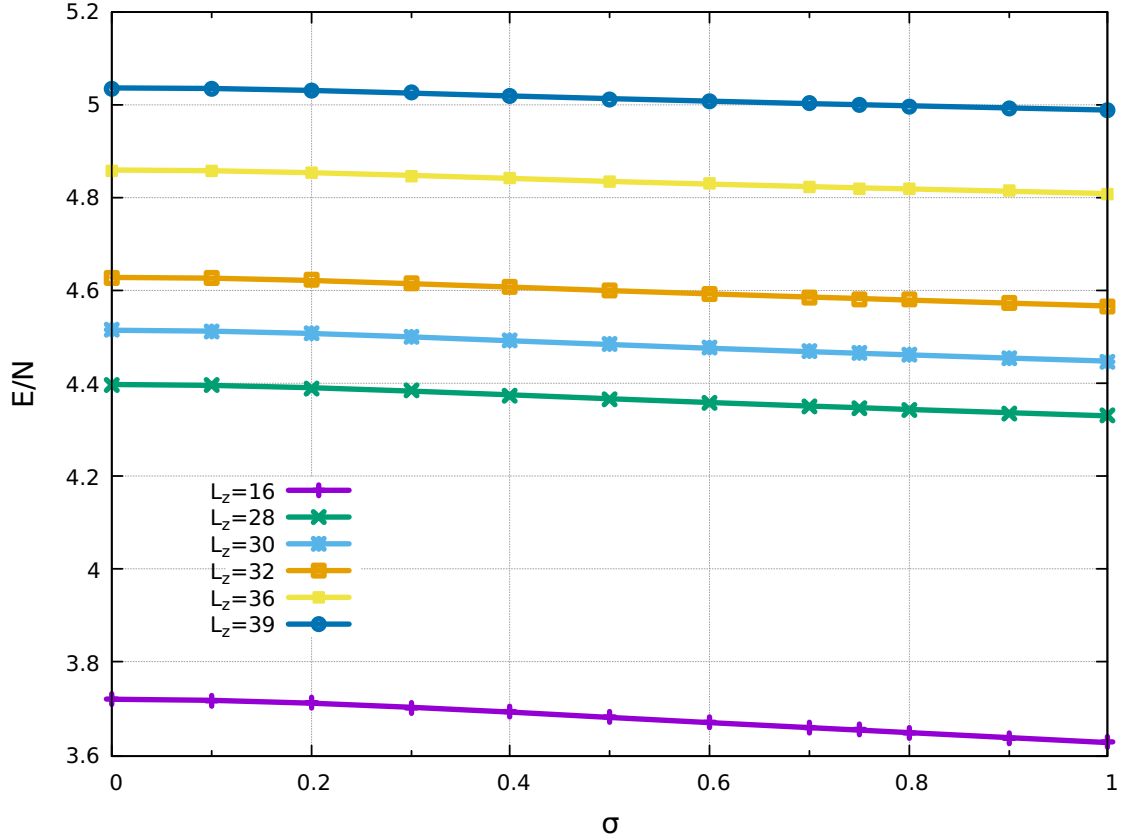


FIG. 5. (Color online) The energy per particle E/N vs the interaction range σ with interaction strength $g_2 = 0.9151$, for $N = 16$ bosons for some of the total angular momentum states, namely, $L_z = 16, 28, 30, 32, 36, 39$. We observe a decrease in ground state energy per particle with increase in interaction range σ .

decreases with increase in σ and takes the least value at $\sigma = 1$, crossing the states $L_z = 28, 30, 36, 39$ at the values of interaction range $\sigma = 0.80, 0.90, 0.60, 0.50$, respectively, as seen in Fig. 4. It is to be noted that two-vortex the $L_z = 32$ state is unique in that it exhibits merging of cores of vortices for values of interaction range $\sigma > 0.75$ as seen in Fig. 9(d). We also observe that there is bunching of two-vortex

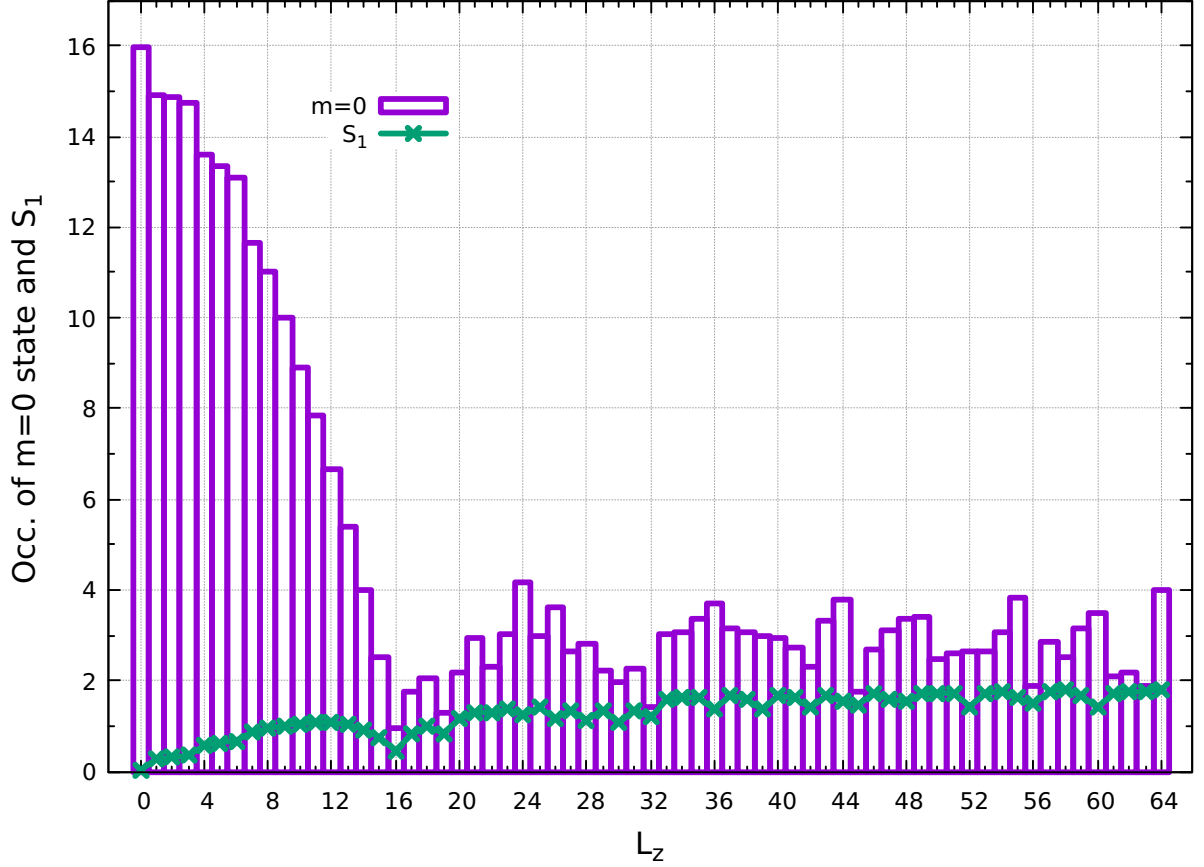


FIG. 6. (Color online) For $N = 16$ spinless bosons, the OPRDM occupations of one-particle angular momentum $m = 0$ state and von Neumann entropy $S_1(L_z, \sigma)$ vs the total angular momentum in the range $0 \leq L_z \leq 64$ with interaction range $\sigma = 0.75$ and interaction strength $g_2 = 0.9151$.

states $L_z = 28$ and $L_z = 30$ with crossing in von Neumann entropy $S_1(L_z, \sigma)$ at the interaction range $\sigma = 0.40$ i.e. $S_1(L_z = 28, \sigma < 0.4) < S_1(L_z = 30, \sigma < 0.4)$ and $S_1(L_z = 28, \sigma > 0.4) > S_1(L_z = 30, \sigma > 0.4)$. Similarly, there is another bunching of three-vortex states $L_z = 36$ and $L_z = 39$ with crossing in von Neumann

entropy $S_1(L_z, \sigma)$ at the interaction range $\sigma = 0.70$ i.e. $S_1(L_z = 36, \sigma < 0.7) < S_1(L_z = 39, \sigma < 0.7)$ and $S_1(L_z = 36, \sigma > 0.7) > S_1(L_z = 39, \sigma > 0.7)$. We observe in Fig. 4 that for the angular momentum $L_z = 30, 39$ states, the von Neumann entropy $S_1(L_z, \sigma)$ remains more or less constant upto the interaction range $\sigma = 0.40$ and then decreases with increase in σ . This decrease in $S_1(L_z, \sigma)$ with increase in σ leads to increase in quantum entanglement between the particles in the condensate. It is to be noted that the angular momentum states $L_z = 30$ and $L_z = 39$ which are meta-stable states for $\sigma = 0.30, 0.50$ become stable states for $\sigma = 0.75$ as shown in Table IV. The above observation can be attributed to the enhancement in quantum entanglement (many-body effects) with increase in interaction range σ .

In Fig. 5, we present the ground state energy per particle E/N with interaction range σ for some of the stable total angular momentum L_z states in Table IV. It is observed that $E(L_z, \sigma') > E(L_z, \sigma)$ for $\sigma' > \sigma$ and $E(L'_z, \sigma) > E(L_z, \sigma)$ for $L'_z > L_z$ in the interval $0 \leq \sigma \leq 1$ hence there is no crossing of energy levels as σ is varied.

In Fig. 6, we present the von Neumann entropy $S_1(L_z, \sigma)$ and the occupation of the non-rotating one-particle angular momentum $m = 0$ state of OPRDM *vs* the total angular momentum in the regime $0 \leq L_z \leq 64$. For the angular momentum range $0 \leq L_z \leq N$, the occupation of $m = 0$ state decreases monotonically with increase in the angular momentum L_z and becomes minimum for the single-vortex state $L_z = N = 16$. At angular momentum $L_z = 0$, the von Neumann entropy $S_1(L_z, \sigma)$ has minimum value whereas the occupation of $m = 0$ state has maximum value which indicates the maximally entangled $L_z = 0$ state. With further increase in angular momentum L_z , the system goes from one stable-state to another stable-state passing through the intervening meta-stable states leading to change in the occupation of one-particle angular momentum state $m = 0$. With increase in angular momentum L_z , we observe that the $m = 0$ state (the core) for the single-vortex $L_z = N$ state has least occupation followed by the second-vortex $L_z = 32$ state. Among the angular

momenta, some of the angular momentum states like $L_z = 0, 16, 32, 42, 45, 56$ have minimum value both in the von Neumann entropy $S_1(L_z, \sigma)$ and the occupation of $m = 0$ state. In the angular momentum regime $L_z > 2N$, the variation in the occupation of $m = 0$ state and the von Neumann entropy $S_1(L_z, \sigma)$ is relatively constant in comparison to the $L_z < N$ state.

D. Internal structure of the condensate: conditional probability distribution

To examine the internal structure of the ground state of the condensate, as seen in the body-fixed frame, we calculate the conditional probability distribution (CPD) [54–56, 72]. The CPD is an experimentally observable quantity which is a measure of the density distribution in the body-fixed frame, defined as the probability of finding a boson at \mathbf{r} given that the other is at \mathbf{r}_0 [73, 74]:

$$\mathcal{P}(\mathbf{r}, \mathbf{r}_0) = \frac{\langle \Psi | \sum_{i \neq j} \delta(\mathbf{r} - \mathbf{r}_i) \delta(\mathbf{r}_0 - \mathbf{r}_j) | \Psi \rangle}{(N-1) \sum_j \langle \psi | \delta(\mathbf{r}_0 - \mathbf{r}_j) | \Psi \rangle} \quad (14)$$

where $|\Psi\rangle$ represents the many-body ground-state obtained through exact diagonalization and $\mathbf{r}_0 = (x_0, y_0)$ is the reference point in the x - y plane (in units of a_\perp). For small values of angular momentum $0 \leq L_z \leq 2N$, the reference point is chosen to take significantly large value i.e. $\mathbf{r}_0 = (3, 0)$. However, in the angular momentum regime $2N < L_z \leq 4N$, the reference point is chosen to be $\mathbf{r}_0 = (1.5, 0)$ [41]. The CPD is depicted through contour plot which is the iso-surface density profile viewed along z -axis in the body-fixed frame.

In the following, we discuss the nucleation of single-vortex state $L_z = N$ followed by multi-vortex states and their structures. We observe that the number of vortices are proportional to the vorticity m^1 given in Table. I (column 2).

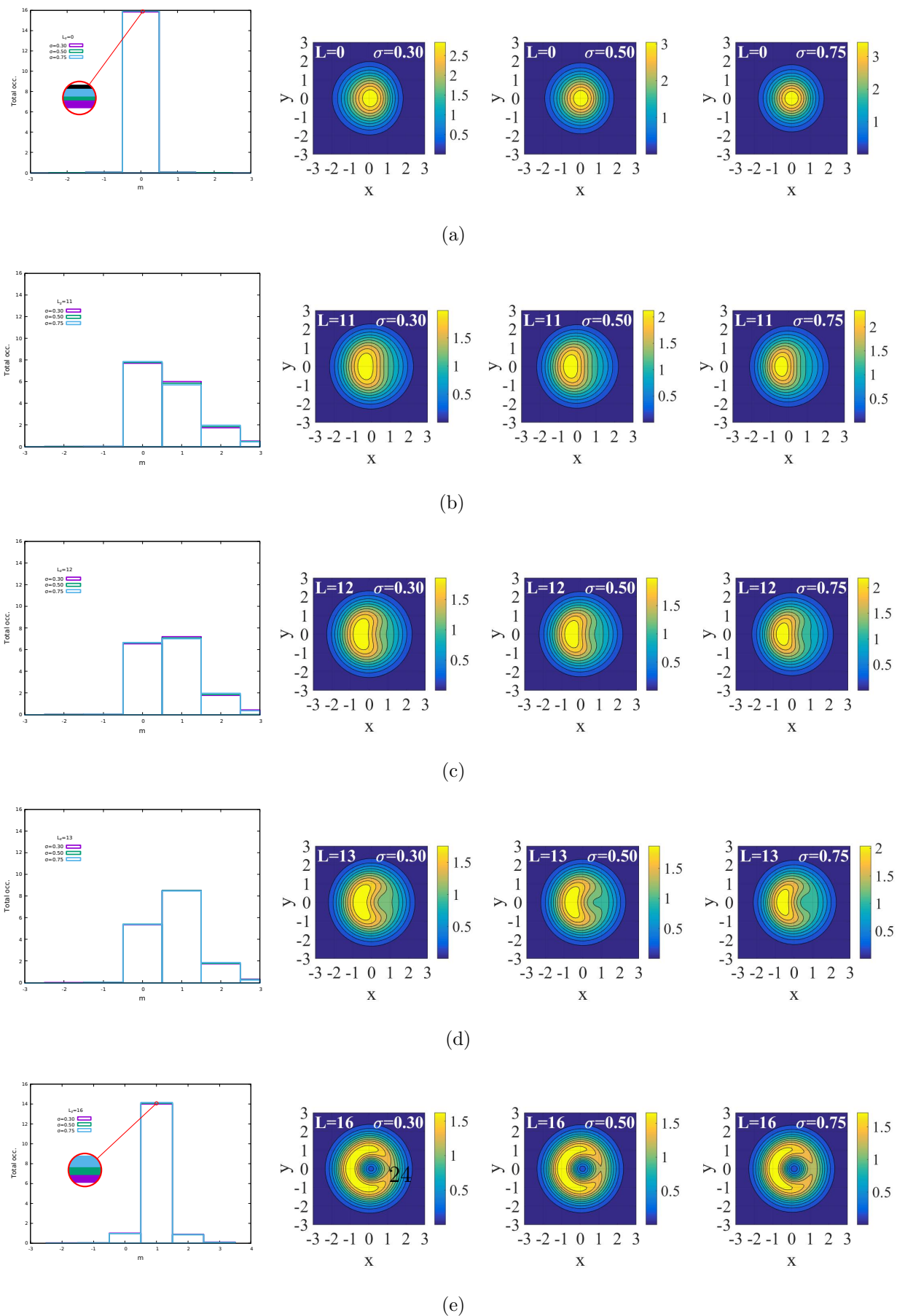


FIG. 7. (Color online) The occupations of one-particle angular momentum states of OPRDM *vs* one-particle angular momentum m and the corresponding CPD plots depict-

E. Single-vortex state

In this subsection, we present contour plots to depict the nucleation of single-vortex state $L_z = N = 16$ in the total angular momentum regime $0 \leq L_z \leq N$ for different values of interaction range $\sigma = 0.30, 0.50, 0.75$ along with the occupations of one-particle angular momentum state m of OPRDM as shown in Fig. 7. The non-rotating $L_z = 0$ state shows a Gaussian-symmetric density profile with vorticity $m^1 = 0$. It is observed that the density profile becomes narrower in width and increases in height with an increase in interaction range σ . For $L_z = 0$ state, the occupation of one-particle angular momentum $m = 0$ state of OPRDM is maximum and increases with increase in interaction range σ as shown in Fig. 7(a). With increase in angular momentum in the regime $0 \leq L_z \leq 16$, the occupation of one-particle angular momentum $m = 0$ state of OPRDM decreases whereas the occupation of one-particle angular momentum $m = 1$ state of OPRDM increases and becomes maximum at $L_z = 16$ as shown in Fig. 7(e). For the angular momentum $L_z = 11$ state, the occupation of one-particle angular momentum $m = 0$ state of OPRDM is greater than the occupation of one-particle angular momentum $m = 1$ state *i.e.* $Ocp(L_z, m = 0) > Ocp(L_z, m = 1)$ for $L_z = 11$, as shown in Fig. 7(b). However, for $L_z = 12$ state, the occupation of one-particle angular momentum $m = 1$ state of OPRDM becomes greater than the occupation of one-particle angular momentum $m = 0$ state *i.e.* $Ocp(L_z, m = 1) > Ocp(L_z, m = 0)$ for $L_z = 12$, as shown in Fig. 7(c). The single-vortex state appears at angular momentum $L_z = N = 16$ as shown in the $L_z - \Omega$ stability graph in Fig. 1. This corresponds to the minima in the von Neumann entropy $S_1(L_z, \sigma)$ as shown in Fig. 3. The single-vortex state emerges through the breaking of Gaussian-symmetry of the density profile as the total angular momentum increases in the regime $0 \leq L_z \leq N$. The entry of the single-vortex state takes place from the periphery along the direction $(x_0, 0)$ [41, 72]. For single-vortex state,

the occupation of one-particle angular momentum $m = 1$ state of OPRDM increases with increase in the interaction range σ as shown in the inset. With increase in the occupation of one-particle angular momentum $m = 1$ state of OPRDM, the contours of the nucleating vortex become visibly sharper, as shown in Figs. 7(b)-7(e), due to an enhancement of the effect of Bose-Einstein statistics. The jump in the occupation of one-particle angular momentum state m of OPRDM from $0 \rightarrow 1$ corresponds to the nucleation of single-vortex state from zero-vortex state [75].

With further increase in angular momentum in the regime $N \leq L_z \leq 4N$, multiple vortices appear [69, 72, 77]. These vortices arrange themselves in geometries like an equilateral triangle, a square and a pentagon for three, four and five vortices, respectively [18, 41, 76]. These vortex configurations are stable due to the effective repulsive interaction experienced by the vortices rotating in the same direction carrying the same ‘charge’ [76].

F. Two-vortex states: merging of vortex-cores

To study the nucleation of two-vortex state in the angular momentum regime $N \leq L_z \leq 2N$, we present CPD plots and occupations of one-particle angular momentum state m of OPRDM in Fig. 9. Beyond the single-vortex $L_z = N = 16$ state, the occupation of one-particle angular momentum state $m = 1$ of OPRDM decreases, as shown in 7(e), whereas for $L_z = 17$ state, the occupation of one-particle angular momentum state $m = 2$ of OPRDM increases, as shown in Fig. 8. The two-vortex state begins to nucleate at angular momentum $L_z = 26$. For the angular momentum $L_z = 26, 28$ states, the occupation of the one-particle angular momentum $m = 2$ state of OPRDM decreases with increase in interaction range σ , *i.e.* $Ocp(m = 2, \sigma') < Ocp(m = 2, \sigma)$ for $\sigma' > \sigma$ in Fig. 9(a)-9(b). However, for the angular momentum $L_z = 30, 32$ states, the occupation of the one-particle angular

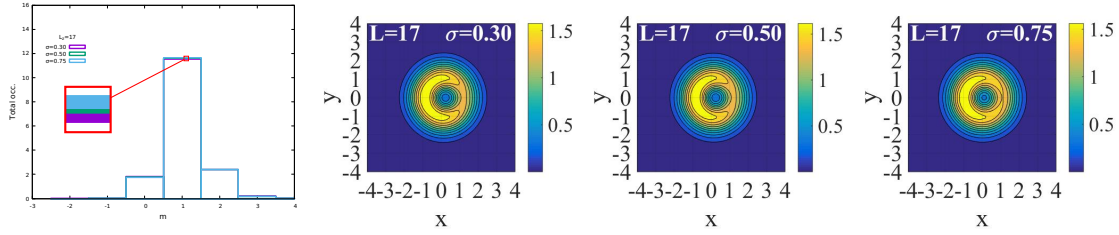


FIG. 8. (Color online) The occupations of one-particle angular momentum states of OPRDM *vs* one-particle angular momentum m and the corresponding CPD plots depicting the single-vortex for $N = 16$ bosons with interaction strength $g_2 = 0.9151$ and three values of interaction range $\sigma = 0.30, 0.50, 0.75$. The reference point has been chosen at $\mathbf{r}_0 = (3, 0)$. In CPD, yellow represents the highest probability density region and blue the least density region in the adjoining color bar: with increase in the angular momentum $L_z > 16$, the occupation maximally occupied one-particle angular momentum state $m = 1$ of OPRDM decreases with respect to $L_z = N$ state as shown in Fig. 7(e). However, with increase in interaction range σ , the occupation maximally occupied one-particle angular momentum state $m = 1$ of OPRDM increases whereas, in the CPD plots, the values of probability density at the peaks increases and at the cores decreases.

momentum $m = 2$ state of OPRDM increases with increase in interaction range σ , *i.e.* $Ocp(m = 2, \sigma') > Ocp(m = 2, \sigma)$ for $\sigma' > \sigma$ as shown in Fig. 9(c)-9(d). It is to noted that the angular momentum $L_z = 26, 28$ are the meta-stable sates whereas $L_z = 30, 32$ are the stable states as seen from the $L_z - \Omega$ stability graph in Fig. 1.

For the two-vortex state with angular momentum $L_z = 2N$, the core of vortices are diagonally placed across the centre of the trap. With increase in interaction range σ , we observe merging of the cores of two-vortex state [21, 26] forming effectively a single-vortex as seen in Fig. 10-12, for $N = 10, 12, 16$ in the subspace of the total angular momentum states $L_z = 2N = 20, 24, 32$ respectively in the beyond Lowest-

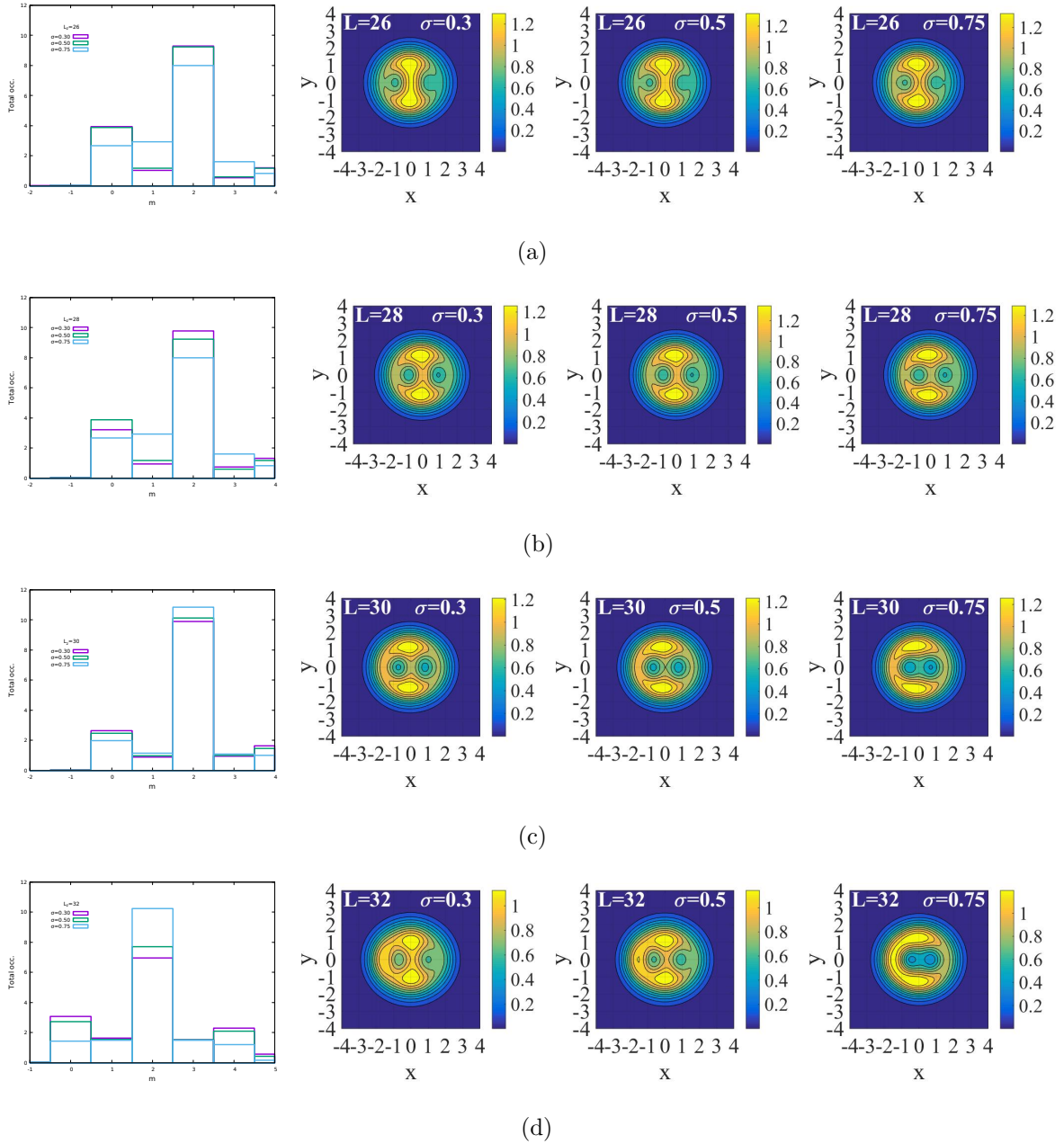


FIG. 9. (Color online) The occupations of one-particle angular momentum states of OPRDM *vs* one-particle angular momentum m and the corresponding CPD plots depicting diagonally symmetric two-vortex state for $N = 16$ bosons with the interaction strength $g_2 = 0.9151$ and the interaction range $\sigma = 0.30, 0.50, 0.75$. The reference point has been chosen at $\mathbf{r}_0 = (3, 0)$. In CPD plots, yellow represents the highest probability density region and blue the least probability density region as shown on the adjoining color bar: With increase in interaction range σ , the contours of two-vortex state becomes visibly sharper. (a) the two-vortex state at $L_z = 26$, with increase in interaction range σ , the occupation of maximally occupied one-particle angular momentum state $m = 2$ of OPRDM decreases whereas, in the CPD plots, the values of probability density at the peaks decrease and at

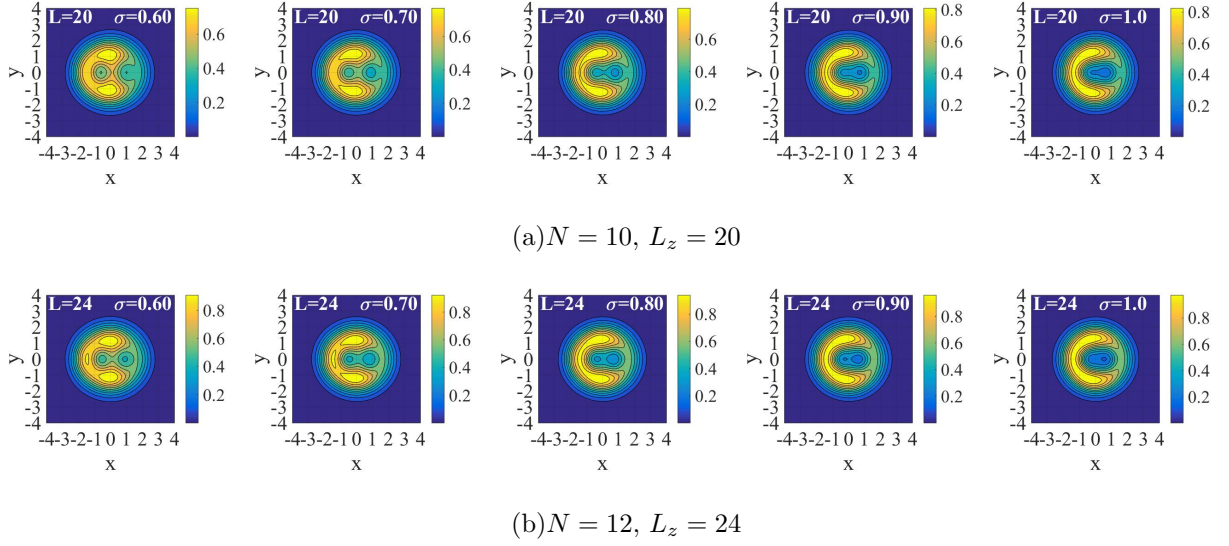


FIG. 10. (Color online) Merging of vortex cores with increase in interaction range: CPD plots depicting diagonally symmetric two-vortex state for $N = 10, 12, 16$ bosons with $g_2 = 0.9151$ and $\sigma = 0.60 - 1.0$ in the beyond Lowest-Landau Level approximation. The reference point has been chosen at $\mathbf{r}_0 = (3, 0)$. In CPD plots, yellow represents the highest probability density region and blue the least probability density region as shown on the adjoining color bar: (a) at $L_z = 2N = 20$, with increase in interaction range beyond $\sigma = 0.6$, the cores begin to merge at $\sigma = 0.80$ and overlap of cores becomes significant. (b) similarly for $L_z = 2N = 24$ state, with increase in interaction range beyond $\sigma = 0.7$, the cores begin to merge at $\sigma = 0.80$ and overlap of cores becomes significant.

Landau Level approximation. Similar vortex-cores merging pattern is observed for $N = 20, 24$ bosons in the subspace of the total angular momentum $L_z = 2N = 40, 48$ in the Lowest-Landau Level approximation as shown in Fig. 12. For a given total angular momentum $L_z = 2N = 32$ state for $N = 16$, the occupation of one-particle angular momentum $m = 2$ state of OPRDM increases consistently with increase in interaction range σ as shown in Fig. 11 which may led the the merge of vortex cores. However, for the vortex states comprising of more than two vortex cores, we do not

observe the vortex cores merging. This is due to the presence of the density peak at the centre of the trap which prevents the cores from merging.

It is further observed that, in the moderately to weakly interacting regime, there is no significant change in the occupation of the maximally occupied one-particle angular momentum $m = 2$ state of OPRDM for $g_2 = 0.9151$ and $g_2 = 0.09151$ as shown in Fig. 9(d) and Fig. 13(a), respectively. However, in the strongly interacting regime, instead of $m = 2$ state, the occupation of $m = 3$ state becomes the maximally occupied one-particle angular momentum state of OPRDM as shown in Fig. 13(b) for $g_2 = 9.151$.

Thus, for a particular angular momentum L_z state, an increase in interaction strength g_2 beyond a certain value changes the occupation of maximally occupied one-particle angular momentum state m of OPRDM to $m' = m + 1$ state. Whereas, an increase in interaction range σ leads to an increase in the occupation of maximally occupied one-particle angular momentum state m of OPRDM for stable states and a decrease in the occupation of maximally occupied one-particle angular momentum state m of OPRDM for meta stable states.

G. Multi-vortex states

In the angular momentum regime $2N < L_z \leq 4N$, with increase in angular momentum L_z , the 3, 4, 5, \dots -fold symmetric vortical states nucleate and arrange themselves in regular patterns as shown in Fig. 14-16. In the angular momentum regime $35 \leq L_z \leq 39$, the occupation of one-particle angular momentum state $m = 3$ of OPRDM increases with increase in angular momentum L_z and becomes maximum for $L_z = 39$, whereas the occupation of one-particle angular momentum state $m = 0$ of OPRDM decreases as shown in Fig. 14. For the angular momentum $L_z = 35$ meta-stable state, the occupation of the one-particle angular momentum

$m = 3$ state of OPRDM decreases with increase in interaction range σ as shown in Fig. 14(a) *i.e.* $Ocp(m = 3, \sigma') < Ocp(m = 3, \sigma)$ for $\sigma' > \sigma$. For the stable angular momentum states $L_z = 36, 39$, the occupation of the one-particle angular momentum $m = 3$ state of OPRDM increases with increase in interaction range σ *i.e.* $Ocp(m = 3, \sigma') > Ocp(m = 3, \sigma)$ for $\sigma' > \sigma$ as shown in Fig. 14(b)-14(c). For the meta-stable $L_z = 35$ angular momentum state, the occupation of one-particle angular momentum state is distributed among all the one-particle angular momentum $m = 0, 1, 2, 3, 4, 5$ states. However, as seen in Fig. 14(b)-14(c), with increase in angular momentum to $L_z = 36, 39$ for stable states, the occupation of maximally occupied one-particle angular momentum $m = 3$ state of OPRDM increases due to the Bose-Einstein statistics. The second maximally occupied state is the one-particle angular momentum $m = 0$ state which forms the core of the vortices. Particles in $m = 0$ state contribute zero to the energy and help minimize the energy. We observe triangular vortical states both for $L_z = 36$ and $L_z = 39$, as shown in Figs. 14(b) and 14(c) respectively. In a uniform system with translational invariance, this triangular lattice will become the building block for the regular Abrikosov lattice [17, 78] in the thermodynamic limit.

Four-vortex state is observed for both angular momentum $L_z = 48, 52$ as shown in Fig. 15. There is an increase in the occupation of one-particle angular momentum $m = 4$ state of OPRDM with increase in the angular momentum regime $48 \leq L_z \leq 52$. Further, for $L_z = 48$ state, there is decrease in the occupation of maximally occupied $m = 4$ state of one-particle angular momentum with increase in interaction range σ as seen in Fig. 15(a) *i.e.* $Ocp(m = 4, \sigma') < Ocp(m = 4, \sigma)$ for $\sigma' > \sigma$. However, for $L_z = 52$ state, the occupation of maximally occupied $m = 4$ state of one-particle angular momentum becomes comparable *i.e.* $Ocp(m = 4, \sigma = 0.30) \sim Ocp(m = 4, \sigma = 0.50) \sim Ocp(m = 4, \sigma = 0.75)$ as seen in Fig. 15(b).

Further increase in angular momentum L_z leads to the nucleation of five-fold sym-

metric vortex state at $L_z = 60$ as seen in Fig. 16. The occupation of the maximally occupied one-particle angular momentum $m = 5$ state of OPRDM increases with increase in the interaction range σ *i.e.* $Ocp(m = 5, \sigma') > Ocp(m = 5, \sigma)$ for $\sigma' > \sigma$.

H. Effects of interaction range σ and number of particles N on the condensate fraction

From Table V, for the angular momentum $L_z = 2N = 32$ state, we observe that the value of the largest condensate fraction increases with increase in interaction range σ *i.e.* $\lambda_1(\sigma') > \lambda_1(\sigma)$ for $\sigma' > \sigma$. As seen from the occupancies of the one-particle states in OPRDM, there is significant rearrangement in the active Fock-space with increase in σ for the interaction range regime $0.6 \leq \sigma \leq 0.75$. The occupancies of various single-particle states (n_i, m_i) , $i = 1, \dots, 5$ of OPRDM change with increase in σ for the angular momentum state $L_z = 32$: $[(2, 2), (0, 0), (4, 4), (1, 1), (3, 3)]_{(\sigma=0.30)} \longrightarrow [(2, 2), (0, 0), (4, 4), (3, 3), (1, 1)]_{(\sigma=0.60)} \longrightarrow [(2, 2), (3, 3), (1, 1), (0, 0), (4, 4)]_{(\sigma=0.75)} \longrightarrow [(2, 2), (1, 1), (3, 3), (0, 0), (4, 4)]_{(\sigma=0.80)}$. Which may be the signature of quantum phase transition induced by interaction range σ .

Further from Table VI, we observe that, with increase in the number of particles N , for a given value of σ , the largest condensate fraction $\lambda_1(N, L_z, \sigma)$ decreases for the non-rotating $L_z = 0$ state and increases for the single-vortex $L_z = N$ state *i.e.*

$$\begin{aligned} \lambda_1(N, L_z = 0) &< \lambda_1(N', L_z = 0) \quad \text{for } N > N' \\ \lambda_1(N, L_z = N) &> \lambda_1(N', L_z = N') \quad \text{for } N > N'. \end{aligned}$$

We further observe from Table VI that for both the non-rotating state and the single-vortex state, the largest condensate fraction $\lambda_1(N, L_z, \sigma)$ increases with increase in interaction range σ whereas the second largest condensate fraction $\lambda_2(N, L_z, \sigma)$ de-

creases with increase in σ . Similar trends as described above is observed for interaction strength $g_2 = 0.09151$ as shown in Table VII. The complete results presented in this work are summarised in the tabular form in the supplementary materiel.

IV. SUMMARY AND CONCLUSION

In summary, we present exact diagonalization study on the ground state of a system of $N = 10, 12, 16, 20, 24$ spinless bosons in the angular momentum regime $0 \leq L_z \leq 4N$ for values of interaction range $\sigma = 0.30, 0.50, 0.75$ and interaction strength $g_2 = 0.9151$ in the Gaussian potential. It is found [35, 53] that the critical angular velocity $\{\Omega_{c_i}(\sigma), i = 1, 2, 3, \dots\}$ decreases with increase in interaction strength and the number of particles. In contrast, we find through our present study that an increase in interaction range σ leads to increase in the critical angular velocity $\{\Omega_{c_i}(\sigma)\}$. We further observe that the span of plateaus on the stability graph L_z vs Ω decreases with increase in σ . Some of the angular momentum states which are meta-stable at small values of σ , evolve into stable states as σ is increased beyond a critical value. Further, with increase in interaction range σ , there is an increase in the value of the largest eigenvalue $\lambda_1(\sigma)$ of OPRDM which is the largest condensate fraction. For the non-rotating $L_z = 0$ state, the largest condensate fraction λ_1 decreases with increase in number of particles N whereas for the first vortex $L_z = N$ state, λ_1 increases with increase in N . For both the non-rotating state and the single-vortex state, the largest condensate fraction λ_1 increases increase whereas the second largest condensate fraction λ_2 decreases, with increase in σ . For the two-vortex $L_z = 2N = 32$ state, with increase in interaction strength g_2 beyond a certain value in the strongly interacting regime, the maximally occupied one-particle angular momentum state of OPRDM changes to m to $m+1$. As a signature of quantum phase transition, a significant rearrangement in the active Fock-space is observed as inter-

action range σ is increased. For stable angular momentum states, with increase in interaction range σ , the occupation of maximally occupied one-particle angular momentum state $m (\neq 0)$ of OPRDM increases whereas the occupation of non-rotating $m = 0$ state decreases. However, for the meta-stable, the occupations of one-particle angular momentum state m of OPRDM is spread over all one-particle angular momentum states. A decrease in von Neumann entropy $S_1(N, L_z, \sigma)$ is observed with increase in σ . We observe crossings in von Neumann entropy $S_1(N, L_z, \sigma)$ with variation in σ among different stable and meta-stable angular momentum states. With increasing angular momentum L_z , more number of quantized vortices appear as the system goes from one stable state to another, forming regular patterns of 2, 3, 4, 5-fold symmetric vortex state. The two-vortex state $L_z = 2N$, has the geometry of two vortices placed symmetrically on the diameter of a circle with its centre coinciding with the centre of the trap. The cores of vortices of the two-vortex state merge with increase in interaction range σ . However, for the vortex states comprising of more than two vortices, we do not observe merging of vortex cores. The single-vortex state is significantly more stable than the multi-vortex states. Among the multi-vortex states, the three-vortex state is more stable in comparison to the two-vortex state. For the stable angular momentum states, the occupation of maximally occupied one-particle angular momentum state m of OPRDM increases with increase in interaction range σ , resulting in increase in density peak and narrowing in width. Further work is in progress to study the effects of three-body Gaussian interaction, in addition to two-body Gaussian interaction, on the ground state of Bose-Einstein Condensate. It is anticipated that even a small three-body interaction will significantly alter the ground state of the many-body system [79].

ACKNOWLEDGEMENT

We thank Mohd. Imran and Mohd Talib for useful comments on the manuscript.

Appendix A: One-particle reduced density in beyond Lowest Landau Level approximation

The variationally obtained many-particle wavefunction for a given number of particles N in a given subspace of angular momentum L_z is given by

$$\begin{aligned}
 |\Psi_{N,L_z}\rangle &= \sum_{\nu} C_{\nu} |\nu; N, L_z\rangle \\
 &= \sum_{\substack{\nu_1, \nu_2, \dots, \nu_M \\ \sum_{\alpha} \nu_{\alpha} = N; \sum_{\alpha} \nu_{\alpha} m_{\alpha} = L_z}} C_{\nu_1, \nu_2, \dots, \nu_M} |\nu_1, \nu_2, \dots, \nu_M\rangle \\
 \text{where } |\nu_1, \nu_2, \dots, \nu_M\rangle &= \frac{(a_1^{\dagger})^{\nu_1} (a_2^{\dagger})^{\nu_2} \dots (a_M^{\dagger})^{\nu_M}}{\sqrt{\nu_1! \nu_2! \dots \nu_M!}} |0\rangle.
 \end{aligned} \tag{A1}$$

The one-particle density operator in the first quantization is defined as:

$$n(\mathbf{r}) = \sum_{i=1}^N \delta(\mathbf{r} - \mathbf{r}_i)$$

where N is number of particles. In the second quantized form, this is given as:

$$\begin{aligned}
 \hat{n}(\mathbf{r}) &= \int d\mathbf{r}' \hat{\Psi}^{\dagger}(\mathbf{r}') \delta(\mathbf{r} - \mathbf{r}') \hat{\Psi}(\mathbf{r}') \\
 &= \hat{\Psi}^{\dagger}(\mathbf{r}) \hat{\Psi}(\mathbf{r}) = \sum_{\mathbf{n}', \mathbf{n}=1}^M u_{\mathbf{n}'}^*(\mathbf{r}) u_{\mathbf{n}}(\mathbf{r}) a_{\mathbf{n}'}^{\dagger} a_{\mathbf{n}}
 \end{aligned}$$

where M is the number of one-particle basis states with composite quantum number $\mathbf{n} \equiv (n_r, m)$. In the Lowest Landau Level approximation, $n_r = 0$ and the one-particle

basis state is labelled by only the angular momentum quantum number $\mathbf{n} \equiv (0, m)$. The expectation value of the number-density operator over the many-particle state $|\Psi_{N,L_z}\rangle$ is given by:

$$\begin{aligned}
n(\mathbf{r}) &= \langle \Psi_{N,L_z} | \hat{n}(\mathbf{r}) | \Psi_{N,L_z} \rangle \\
&= \sum'_{\nu'} \sum'_{\nu} C_{\nu'}^* C_{\nu} \langle \nu' | \sum_{\mathbf{n}', \mathbf{n}} u_{\mathbf{n}'}^*(\mathbf{r}) u_{\mathbf{n}}(\mathbf{r}) a_{\mathbf{n}}^\dagger a_{\mathbf{n}} | \nu \rangle \\
&= \sum'_{\nu'} \sum'_{\nu} \sum_{\mathbf{n}', \mathbf{n}} u_{\mathbf{n}'}^*(\mathbf{r}) u_{\mathbf{n}}(\mathbf{r}) C_{\nu'}^* C_{\nu} \\
&\quad \langle \nu'_1 \nu'_2 \cdots \nu'_M | a_{\mathbf{n}}^\dagger a_{\mathbf{n}} | \nu_1 \nu_2 \cdots \nu_M \rangle \\
&= \sum_{\mathbf{n}', \mathbf{n}} u_{\mathbf{n}'}^*(\mathbf{r}) u_{\mathbf{n}}(\mathbf{r}) \sum'_{\nu'_1 \cdots \nu'_n \cdots \nu'_M} \sum'_{\nu_1 \cdots \nu_n \cdots \nu_M} \\
&\quad C_{\nu'_1 \cdots \nu'_n \cdots \nu'_M}^* C_{\nu_1 \cdots \nu_n \cdots \nu_M} \\
&\quad \langle 0 | \frac{(a_1)^{\nu'_1} \cdots (a_{\mathbf{n}'})^{\nu'_n} \cdots (a_{\mathbf{n}})^{\nu'_n} \cdots (a_M)^{\nu'_M}}{\sqrt{\nu'_1! \cdots \nu'_n! \cdots \nu'_n! \cdots \nu'_M!}} | a_{\mathbf{n}}^\dagger a_{\mathbf{n}} \rangle \\
&\quad \frac{(a_1^\dagger)^{\nu_1} \cdots (a_{\mathbf{n}}^\dagger)^{\nu_n} \cdots (a_{\mathbf{n}'}^\dagger)^{\nu_{n'}} \cdots (a_M^\dagger)^{\nu_M}}{\sqrt{\nu_1! \cdots \nu_n! \cdots \nu_{n'}! \cdots \nu_M!}} | 0 \rangle \\
&= \sum_{\mathbf{n}', \mathbf{n}} u_{\mathbf{n}}^*(\mathbf{r}) u_{\mathbf{n}'}(\mathbf{r}) \\
&\quad \sum'_{\nu'_1 \cdots \nu'_n \cdots \nu'_M} \sum'_{\nu_1 \cdots \nu_n \cdots \nu_M} C_{\nu'_1 \cdots \nu'_n \cdots \nu'_M}^* \\
&\quad C_{\nu_1 \cdots \nu_n \cdots \nu_{n'} \cdots \nu_M} \sqrt{\nu_n(\nu_{n'} + 1)} \delta_{\nu'_1, \nu_1} \cdots \delta_{\nu'_n, \nu_n - 1} \\
&\quad \cdots \delta_{\nu'_n, \nu_{n'} + 1} \cdots \delta_{\nu'_M, \nu_M} \\
&= \sum_{\mathbf{n}' \neq \mathbf{n}} u_{\mathbf{n}'}^*(\mathbf{r}) u_{\mathbf{n}}(\mathbf{r}) \sum_{\nu_1 \cdots \nu_n \cdots \nu_M} C_{\nu_1 \cdots (\nu_n - 1) \cdots (\nu_{n'} + 1) \cdots \nu_M}^* \\
&\quad C_{\nu_1 \cdots \nu_n \cdots \nu_{n'} \cdots \nu_M} \sqrt{\nu_n(\nu_{n'} + 1)}. \\
&+ \sum_{\mathbf{n}} |u_{\mathbf{n}}(\mathbf{r})|^2 \sum_{\nu_1 \cdots \nu_n \cdots \nu_M} \nu_n |C_{\nu_1 \cdots \nu_n \cdots \nu_M}^*|^2
\end{aligned}$$

above Eq. (A2) takes the following form [35]

$$n(\mathbf{r}) = \sum_{n'_r, m} \sum_{n_r, m} \rho_{n'_r, m; n_r, m} u_{n'_r, m}^*(\mathbf{r}) u_{n_r, m}(\mathbf{r}) \quad (\text{A2})$$

which after diagonalization becomes

$$n(\mathbf{r}) = \sum_{\mu} (N\lambda_{\mu}) |\chi_{\mu, m^{\mu}}(\mathbf{r})|^2 \quad (\text{A3})$$

where $\chi_{\mu, m^{\mu}}(\mathbf{r})$ is as defined in Eq. (11). It is clear that the density operator will not exhibit any interference patterns. Eq. (A3) above in the beyond Lowest Landau Level approximation reduces to Eq. (9) in reference [46] in the Lowest Landau Level approximation.

Appendix B: Conditional probability distribution (CPD) in beyond Lowest Landau Level approximation

The conditional probability distribution (CPD) is given by:

$$\mathcal{P}(\mathbf{r}, \mathbf{r}_0) = \sum_{i < j}^N \delta(\mathbf{r} - \mathbf{r}_i) \delta(\mathbf{r}_0 - \mathbf{r}_j)$$

where N is the number of particles. In the second quantized form it is given as:

$$\begin{aligned} \hat{\mathcal{P}}(\mathbf{r}, \mathbf{r}_0) &= \frac{1}{2} \left[\int d\mathbf{r}' d\mathbf{r}'' \right] \Psi^{\dagger}(\mathbf{r}') \Psi^{\dagger}(\mathbf{r}'') \\ &\times (\delta(\mathbf{r} - \mathbf{r}') \delta(\mathbf{r}_0 - \mathbf{r}'') + \delta(\mathbf{r} - \mathbf{r}'') \delta(\mathbf{r}_0 - \mathbf{r}')) \\ &\times \Psi(\mathbf{r}'') \Psi(\mathbf{r}') \\ &= \Psi^{\dagger}(\mathbf{r}) \Psi^{\dagger}(\mathbf{r}_0) \Psi(\mathbf{r}_0) \Psi(\mathbf{r}) \\ &= \sum_{\mathbf{n}', \mathbf{n}} \sum_{\mathbf{m}', \mathbf{m}} u_{\mathbf{n}'}^*(\mathbf{r}) u_{\mathbf{n}}(\mathbf{r}) u_{\mathbf{m}'}^*(\mathbf{r}_0) u_{\mathbf{m}}(\mathbf{r}_0) \\ &\quad a_{\mathbf{n}'}^{\dagger} a_{\mathbf{m}'}^{\dagger} a_{\mathbf{m}} a_{\mathbf{n}}. \end{aligned}$$

The expectation value of CPD operator over the many-particle state $|\Psi_{N,L_z}\rangle$ defined in Eq. (A1) above is given as:

$$\begin{aligned}
\mathcal{P}(\mathbf{r}, \mathbf{r}_0) &= \langle \Psi_{N,L_z} | \hat{\mathcal{P}}(\mathbf{r}, \mathbf{r}_0) | \Psi_{N,L_z} \rangle \\
&= \langle \Psi_{N,L_z} | \sum_{\mathbf{m}', \mathbf{m}} \sum_{\mathbf{n}', \mathbf{n}} u_{\mathbf{n}'}^*(\mathbf{r}) u_{\mathbf{n}}(\mathbf{r}) u_{\mathbf{m}'}^*(\mathbf{r}_0) u_{\mathbf{m}}(\mathbf{r}_0) \\
&\quad a_{\mathbf{n}'}^\dagger a_{\mathbf{m}'}^\dagger a_{\mathbf{m}} a_{\mathbf{n}} | \Psi_{N,L_z} \rangle \\
&= \sum_{\nu', \nu} C_{\nu'}^* C_{\nu} \sum_{\mathbf{m}', \mathbf{m}} \sum_{\mathbf{n}', \mathbf{n}} u_{\mathbf{n}'}^*(\mathbf{r}) u_{\mathbf{n}}(\mathbf{r}) u_{\mathbf{m}'}^*(\mathbf{r}_0) u_{\mathbf{m}}(\mathbf{r}_0) \\
&\quad \langle \nu' | a_{\mathbf{n}'}^\dagger a_{\mathbf{m}'}^\dagger a_{\mathbf{m}} a_{\mathbf{n}} | \nu \rangle \\
&= \sum_{\mathbf{m}', \mathbf{m}} \sum_{\mathbf{n}', \mathbf{n}} u_{\mathbf{n}'}^*(\mathbf{r}) u_{\mathbf{n}}(\mathbf{r}) u_{\mathbf{m}'}^*(\mathbf{r}_0) u_{\mathbf{m}}(\mathbf{r}_0) \sum_{\nu'_1 \dots \nu'_n \dots \nu'_{\mathbf{m}'}} C_{\nu'_1 \dots \nu'_n \dots \nu'_{\mathbf{m}'}}^* \sum_{\nu_1 \dots \nu_n \dots \nu_{\mathbf{m}}} C_{\nu_1 \dots \nu_n \dots \nu_{\mathbf{m}}} \\
&\quad \langle 0 | \frac{(a_{\mathbf{1}})^{\nu'_1} \dots (a_{\mathbf{n}})^{\nu'_n} \dots (a_{\mathbf{n}'})^{\nu'_{\mathbf{n}'}} \dots (a_{\mathbf{m}})^{\nu'_{\mathbf{m}}} \dots (a_{\mathbf{m}'})^{\nu'_{\mathbf{m}'}} \dots (a_{\mathbf{M}})^{\nu'_{\mathbf{M}}}}{\sqrt{\nu'_1! \dots \nu'_n! \dots \nu'_{\mathbf{n}'!} \dots \nu'_{\mathbf{m}}! \dots \nu'_{\mathbf{m}'!} \dots \nu'_{\mathbf{M}}!}} | a_{\mathbf{n}'}^\dagger a_{\mathbf{m}'}^\dagger a_{\mathbf{m}} a_{\mathbf{n}} | \\
&\quad \frac{(a_{\mathbf{1}}^\dagger)^{\nu_1} \dots (a_{\mathbf{n}}^\dagger)^{\nu_n} \dots (a_{\mathbf{n}'})^{\nu_{\mathbf{n}'}} \dots (a_{\mathbf{m}}^\dagger)^{\nu_{\mathbf{m}}} \dots (a_{\mathbf{m}'})^{\nu_{\mathbf{m}'}} \dots (a_{\mathbf{M}}^\dagger)^{\nu_{\mathbf{M}}}}{\sqrt{\nu_1! \dots \nu_n! \dots \nu_{\mathbf{n}'!} \dots \nu_{\mathbf{m}}! \dots \nu_{\mathbf{m}'!} \dots \nu_{\mathbf{M}}!}} | 0 \rangle \\
\mathcal{P}(\mathbf{r}, \mathbf{r}_0) &= \sum_{\mathbf{m}', \mathbf{m}} \sum_{\mathbf{n}', \mathbf{n}} u_{\mathbf{n}'}^*(\mathbf{r}) u_{\mathbf{n}}(\mathbf{r}) u_{\mathbf{m}'}^*(\mathbf{r}_0) u_{\mathbf{m}}(\mathbf{r}_0) \\
&\quad \sum_{\nu'_n, \nu'_{\mathbf{n}'}, \nu'_{\mathbf{m}}, \nu'_{\mathbf{m}'}} \sum_{\nu_n, \nu_{\mathbf{n}'}, \nu_{\mathbf{m}}, \nu_{\mathbf{m}'}} C_{\nu'_1 \dots \nu'_n \dots \nu'_{\mathbf{n}'}, \nu'_{\mathbf{m}}, \nu'_{\mathbf{m}'}, \nu'_{\mathbf{M}}}^* \\
&\quad C_{\nu_1 \dots \nu_n \dots \nu_{\mathbf{n}'}, \nu_{\mathbf{m}}, \nu_{\mathbf{m}'}, \nu_{\mathbf{M}}} \sqrt{\nu_n \nu_{\mathbf{m}} (\nu_{\mathbf{n}'} + 1) (\nu_{\mathbf{m}'} + 1)} \\
&\quad \delta_{\nu'_n, \nu_n - 1} \delta_{\nu'_{\mathbf{m}}, \nu_{\mathbf{m}} - 1} \delta_{\nu'_{\mathbf{m}'}, \nu_{\mathbf{m}'} + 1} \delta_{\nu'_{\mathbf{n}'}, \nu_{\mathbf{n}'} + 1}
\end{aligned} \tag{B1}$$

$$\begin{aligned}
&= \sum_{\mathbf{m}', \mathbf{m}} \sum_{\mathbf{n}', \mathbf{n}} u_{\mathbf{n}'}^*(\mathbf{r}) u_{\mathbf{n}}(\mathbf{r}) u_{\mathbf{m}'}^*(\mathbf{r}_0) u_{\mathbf{m}}(\mathbf{r}_0) \\
&\quad \sum_{\nu_{\mathbf{n}}, \nu_{\mathbf{n}'}, \nu_{\mathbf{m}}, \nu_{\mathbf{m}'}}^{\prime} C_{\nu_1 \dots (\nu_{\mathbf{n}}-1) \dots (\nu_{\mathbf{n}'}+1) \dots (\nu_{\mathbf{m}}-1) \dots (\nu_{\mathbf{m}'}+1) \dots \nu_M}^* \\
&\quad C_{\nu_1 \dots (\nu_{\mathbf{n}}) \dots (\nu_{\mathbf{n}'}) \dots (\nu_{\mathbf{m}}) \dots (\nu_{\mathbf{m}'}) \dots \nu_M} \\
&\quad \sqrt{\nu_{\mathbf{n}} \nu_{\mathbf{m}} (\nu_{\mathbf{n}'} + 1) (\nu_{\mathbf{m}'} + 1)}.
\end{aligned} \tag{B2}$$

Equation (B2) above is the expression for the conditional probability distribution (CPD) in the beyond Lowest Landau Level approximation, which is the analogue of Eq. (11) in reference [46] in the Lowest Landau Level approximation. Equation (B2) reduces in the Lowest Landau Level approximation with $\mathbf{m}' \equiv (0, m')$, $\mathbf{m} \equiv (0, m)$, $\mathbf{n}' \equiv (0, m'')$, $\mathbf{n} \equiv (0, m''')$ to

$$\begin{aligned}
&= \sum_{m', m} \sum_{m'', m'''} u_{m''}^*(\mathbf{r}) u_{m'''}(\mathbf{r}) u_{m'}^*(\mathbf{r}_0) u_m(\mathbf{r}_0) \\
&\quad \sum_{\nu_{m'''}, \nu_{m''}, \nu_m, \nu_{m'}}^{\prime} C_{\nu_1 \dots (\nu_{m'''}-1) \dots (\nu_{m''}+1) \dots (\nu_m-1) \dots (\nu_{m'}+1) \dots \nu_M}^* \\
&\quad C_{\nu_1 \dots (\nu_{m'''}) \dots (\nu_{m''}) \dots (\nu_m) \dots (\nu_{m'}) \dots \nu_M} \\
&\quad \sqrt{\nu_{m'''} \nu_m (\nu_{m''} + 1) (\nu_{m'} + 1)}.
\end{aligned} \tag{B3}$$

In order to understand the role of reference point \mathbf{r}_0 in Eq. (B3), we consider the following function

$$\begin{aligned}
&u_{m''}^*(\mathbf{r}) u_{m'''}(\mathbf{r}) u_{m'}^*(\mathbf{r}_0) u_m(\mathbf{r}_0) \\
&= \frac{1}{\pi^2} \frac{r^{m''}}{\sqrt{m''!}} \frac{r^{m'''}}{\sqrt{m'''!}} \frac{r_0^{m'}}{\sqrt{m'!}} \frac{r_0^m}{\sqrt{m!}} \\
&e^{i(m-m')\theta_0} e^{i(m''-m'')\theta}
\end{aligned} \tag{B4}$$

It follows from the conservation of angular momentum that $m''' - m'' = -(m - m')$ whereby the angular dependence in equation (B4) becomes

$$\begin{aligned} & \frac{u_{m''}^*(\mathbf{r}) u_{(m''-(m-m'))}(\mathbf{r}) u_{m'}^*(\mathbf{r}_0) u_m(\mathbf{r}_0)}{1} \\ = & \frac{r^{m''}}{\pi^2 \sqrt{m''!}} \frac{r^{(m''-(m-m'))}}{\sqrt{(m''-(m-m'))!}} \frac{r_0^{m'}}{\sqrt{m'!}} \frac{r_0^m}{\sqrt{m!}} \\ & e^{i(m-m')(\theta-\theta_0)} \end{aligned} \quad (\text{B5})$$

The function (B5) above survives for the choice of the reference point $\mathbf{r}_0 = (0, \theta_0)$ only when $m = m' = 0$. For a fixed value of \mathbf{r}_0 , except $\mathbf{r}_0 = 0$, change in θ_0 is the rigid rotation of the function. Any arbitrary change in θ_0 fixes the orientation of spatial correlation. Taking our reference point \mathbf{r}_0 coinciding with the origin (trap centre) *i.e.* $\mathbf{r}_0 = (0, \theta_0)$, Eq. (B3), becomes

$$\begin{aligned} \mathcal{P}(\mathbf{r}, \mathbf{0}) &= |u_0(0)|^2 \nu_0 \\ & \sum_m \underbrace{|u_m(\mathbf{r})|^2 \sum_{\nu_m} \nu_m |C_{\nu_0 \dots \nu_m \dots \nu_{M-1}}|^2}_{(N\lambda_m) |\chi_m(\mathbf{r})|^2} \end{aligned} \quad (\text{B6})$$

i.e. CPD exhibits cylindrical symmetry as shown in Fig. 17 when the reference point \mathbf{r}_0 coincides with the trap centre. The cylindrical symmetry is broken as reference point is moved away from the trap centre. Equation (B6) is the same as Eq. (14) in reference [46].

Appendix C: Anisotropic term in Hamiltonian breaking x - y symmetry in beyond Lowest Landau Level approximation

The potential with anisotropy in x - y plane taken in the first quantized form is :

$$V_p = \frac{A}{2} M \omega_{\perp}^2 \sum_{i=1}^N (x_i^2 - y_i^2) = \frac{A}{2} m \omega_{\perp}^2 \sum_{i=1}^N r_{\perp i}^2 (\text{Cos} 2\phi_i) \quad (\text{C1})$$

where perturbative constant A is dimensionless. perturbative potential energy V_p has dimension of energy and to make it dimensionless we have to divide it by $\hbar\omega_\perp$ i.e. $\frac{1}{2}M\omega_\perp^2 r_\perp^2 \text{Cos}(2\phi)/(\hbar\omega_\perp) = (\frac{1}{2}M\omega_\perp r_\perp^2 \text{Cos}(2\phi))/\hbar = \frac{1}{2}(\alpha_\perp r_\perp)^2 \text{Cos}(2\phi)$. Where $\alpha_\perp r_\perp = \Lambda$ is a dimensionless parameter. Equation (C1) in the second quantized form becomes

$$\begin{aligned}\hat{V}_p &= \frac{A}{2} \int d\mathbf{r} \Psi^\dagger(\mathbf{r}) (\alpha_\perp r_\perp)^2 \text{Cos}(2\phi) \Psi(\mathbf{r}) \\ &= \frac{A}{2} \sum_{\mathbf{n}'} \sum_{\mathbf{n}} a_{\mathbf{n}'}^\dagger a_{\mathbf{n}} \int d\mathbf{r} u_{\mathbf{n}'}^*(\mathbf{r}) (\alpha_\perp r_\perp)^2 \text{Cos}(2\phi) u_{\mathbf{n}}(\mathbf{r})\end{aligned}$$

with $d\mathbf{r} = r_\perp dr_\perp d\phi$. Writing Eq. (C1) in terms of composite quantum numbers $\mathbf{n} \equiv (n_r, m)$ and $\mathbf{n}' \equiv (n'_r, m')$, we get

$$\begin{aligned}\hat{V}_p &= \frac{A}{2} \sum_{n'_r, n_r}^{0,1,2,\dots} \sum_{m', m=-\infty}^{\infty} a_{n'_r, m'}^\dagger a_{n_r, m} \\ &\quad \sqrt{\frac{1}{\pi^2} \frac{n'_r! n_r!}{(n'_r + |m'|)!(n_r + |m|)!}} \\ &\quad \int_{\Lambda=0}^{\infty} \int_{\phi=0}^{2\pi} \frac{1}{2} d\Lambda^2 d\phi L_{n'_r}^{|m'|}(\Lambda^2) L_{n_r}^{|m|}(\Lambda^2) \\ &\quad \Lambda^{|m'|+|m|} e^{-\Lambda^2} e^{i(m-m')\phi} \Lambda^2 \left(\frac{e^{2i\phi} + e^{-2i\phi}}{2} \right)\end{aligned}$$

first we integrating over ϕ which gives δ function

$$\begin{aligned}
\hat{V}_p &= \frac{A}{8\pi} \sum_{n_r, n'_r}^{0,1,2,\dots} \sum_{m, m'=-\infty}^{\infty} 2\pi [\delta_{|m|, |m'|-2} \\
& a_{n'_r, m'}^\dagger a_{n_r, m} \sqrt{\frac{n_r! n'_r!}{(n_r + |m|)! (n'_r + |m'|)!}} \\
& \int_{\Lambda=0}^{\infty} d\Lambda^2 \Lambda^{|m|+|m'|+2} e^{-\Lambda^2} L_{n_r}^{|m|}(\Lambda^2) L_{n'_r}^{|m'|}(\Lambda^2) \\
& + \delta_{|m|, |m'|+2} a_{n'_r, m'}^\dagger a_{n_r, m} \sqrt{\frac{n'_r! n_r!}{(n'_r + |m'|)! (n_r + |m|)!}} \\
& \int_{\Lambda=0}^{\infty} d\Lambda^2 \Lambda^{|m|+|m'|+2} e^{-\Lambda^2} L_{n'_r}^{|m'|}(\Lambda^2) L_{n_r}^{|m|}(\Lambda^2)]
\end{aligned}$$

replacing m with m' using δ -function and rewriting the above equation as

$$\begin{aligned}
\hat{V}_p &= \frac{A}{4} \sum_{n_r, n'_r}^{0,1,2,\dots} \sum_{m'=-\infty}^{\infty} [a_{n'_r, m'}^\dagger a_{n_r, m'-2} \\
& \sqrt{\frac{n_r! n'_r!}{(n_r + |m'| - 2)! (n'_r + |m'|)!}} \\
& \int_{\Lambda=0}^{\infty} e^{-\Lambda^2} \Lambda^{2|m'|} L_{n_r}^{|m'|-2}(\Lambda^2) L_{n'_r}^{|m'|}(\Lambda^2) d\Lambda^2 \\
& + a_{n'_r, m'}^\dagger a_{n_r, m'+2} \sqrt{\frac{n_r! n'_r!}{(n_r + |m'| + 2)! (n'_r + |m'|)!}} \\
& \int_{\Lambda=0}^{\infty} e^{-\Lambda^2} \Lambda^{2(|m'|+2)} L_{n_r}^{|m'|+2}(\Lambda^2) L_{n'_r}^{|m'|}(\Lambda^2) d\Lambda^2]
\end{aligned}$$

expanding the associated Laguerre polynomial in general form as $L_q^k(\Lambda) = \sum_{p=0}^q (-1)^p \frac{(r+k)!}{(q-p)!(k+p)!p!} \Lambda^p$ and follow the integration.

$$\begin{aligned}
\hat{V}_p = & \frac{A}{4} \sum_{n'_r, n_r} \sum_{m'=-\infty}^{\infty} [a_{n'_r, m'}^\dagger a_{n_r, m'-2} \\
& \sqrt{\frac{n'_r! n_r!}{(n'_r + |m'|)!(n_r + |m'| - 2)!}} \\
& \sum_{p=0}^{n_r} (-1)^p \frac{(|m'| + n_r - 2)!}{(n_r - p)!(|m'| + p - 2)!p!} \\
& \sum_{q=0}^{n'_r} (-1)^q \frac{(n'_r + |m'|)!}{(n'_r - q)!(|m'| + q)!q!} (|m'| + p + q)! \\
& + a_{n'_r, m'}^\dagger a_{n_r, m'+2} \sqrt{\frac{n_r! n'_r!}{(n_r + |m'| + 2)!(n'_r + |m'|)!}} \\
& \sum_{p=0}^{n_r} (-1)^p \frac{(n_r + |m'| + 2)!}{(n_r - p)!(|m'| + p + 2)!p!} \\
& \sum_{q=0}^{n'_r} (-1)^q \frac{(|m'| + n'_r)!}{(n'_r - q)!(|m'| + q)!q!} (|m'| + p + q + 2)!]
\end{aligned} \tag{C2}$$

The Eq. (C2) is the beyond Lowest Landau Level approximation analogue of equation (17) in reference [46] in the Lowest Landau Level approximation which can be obtained from Eq. (C2) with $n'_r = n_r = 0$ and $m = 0, 1, 2, \dots$

$$\begin{aligned}
\hat{V}_p = & \frac{A}{4} \sum_{m=0,1,2,\dots} (\sqrt{m(m-1)} a_m^\dagger a_{m-2} \\
& + \sqrt{(m+1)((m+2)} a_m^\dagger a_{m+2})
\end{aligned} \tag{C3}$$

-
- [1] H.J. Metcalf and P. Van der Straten, *Laser Cooling and Trapping*, Springer Verlag, 1999.
- [2] Michèle Leduc, Julien Dugué, and Juliette Simonet, AIP Conference Proceedings **1119**, 37 (2009); <https://doi.org/10.1063/1.3137904>
- [3] L. Pitaevski and S. Stringari, *Bose-Einstein Condensation*, Clarendon Press, (2003).
- [4] See, Proceedings of the International School of Physics “Enrico Fermi,” Course CXL, 1999, edited by M. Inguscio, S. Stringari, C.E. Wieman (IOS Press, Netherlands, 1999).
- [5] H. Feshbach, Ann. Phys. **19** 287 (1962).
- [6] M.H. Anderson, J.R. Ensher, M.R. Matthews, C.E. Wieman, E.A. Cornell, Science **269**, 198 (1995).
- [7] K.B. Davis, M. O. Mewes, M.R. Andrews, N.j. van Druten, D.S. Durfee, D.M. Kurn, and W. Ketterle, Phys. Rev. Lett. **75** 3969 (1995).
- [8] G. Modugno, G. Ferrari, G. Roati, R.J. Brecha, A. Simoni, and M. Inguscio, Science **294** 1320 (2001).
- [9] C.C Bradley, C. A Sackett, J.J. Tollett, and R.G. Hulet, Phys. Rev. Lett. **75**, 1687 (1995).
- [10] N.K. Wilkin, J.M.F. Gunn, and R.A. Smith, Phys. Rev. Lett. **80**, 2265 (1997).
- [11] C.A. Regal, M. Greiner, and D.S. Jin, Phys. Rev. Lett. **92**, 040403 (2004).
- [12] G. Bighin, and Luca Salasnich, Sci. Rep. **7** 45702 (2017).
- [13] M. Greiner, C. A. Regal, and D. S. Jin, Nature **426**, 537 (2003).
- [14] Ulrich Ebling, Ali Alavi, and Joachim Brand, Phys. Rev. Research **3**, 023142 (2021).
- [15] A.J. Leggett, in *Low Temperature Physics*, Lecture Notes in Physics Vol.394, edited by M.J.R. Hoch et al.(Springer-Verlage, Berlin, 1991).

- [16] R.J. Donnelly, *Quantized Vortices in Helium II* (Cambridge University Press, Cambridge, 1991).
- [17] A.A. Abrikosov, *Revs. of Mod Phys.* **76**, 0975 (2004).
- [18] K.W. Madison, F. Chevy, W. Wohlleben, and J. Dalibard, *Phys. Rev. Lett.* **84**, 806 (2000).
- [19] Y.J. Lin, R.L. Compton, K. Jiménez-García, J.V. Porto, and I.B. Spielman, *Nature* **462**, 268 (2009).
- [20] M.R. Matthews, B.P. Anderson, P.C. Haljan, D.S. Hall, C.E. Wieman, and E.A. Cornell, *Phys. Rev. Lett.* **83**, 2498 (1999).
- [21] N.R. Cooper, N.K. Wilkin, and J.M.F. Gunn, *Phys. Rev. Lett.* **87**, 120405 (2001).
- [22] Leslie O. Baksmaty, Constantine Yannouleas, and Uzi Landman, *Phys. Rev. A* **75**, 023620 (2007).
- [23] R.A. Williams, S. Al-Assam, and C.J. Foot, *Phys. Rev. Lett.* **104**, 050404 (2010).
- [24] K. Suthar, A. Roy, and D. Angom, *J. Phys. B: At. Mol. Opt. Phys.* **47** 135301 (2014).
- [25] J. Sinova, C.B. Hanna, and A.H. MacDonald, *Phys. Rev. Lett.* **89**, 030403 (2002).
- [26] Gautam I. Menon, C.Dasgupta, H.R. Krishnamurthy, T.V. Ramakrishnan, and Surajit Sengupta, *Phys. Rev. B.* **54**, 16192 (1996).
- [27] Péter Jeszenszki, Ali. Alavi and Joachin Brand, *Phys. Rev. A* **99**, 033608 (2019).
- [28] T. Busch, B.G. Englert, K. Rzȃzewski and Kazimierz Wilken, *Found. Physics*, **549**, 498 (1998).
- [29] Rostislav A. Doganov, Shachar Klaiman, Ofir E. Alon, Alexej I. Streltsov, and Lorenz S. Cederbaum, *Phys. Rev. A* **87**,033631 (2013).
- [30] S. Inouye, M.R. Andrews, J.Stanger, H.J.Miesner, D.M. Stamper-Kurn and W. Ketterle, *Nature (London)* **392**,(1998) 151.
- [31] A.D.Lange, K.Pilch, A. Pranter, F. Ferlaino, B. Engeser, H.-C. Nägerl, R. Grsimm and C. Chin, *Phys. Rev. A* **79**, 013622 (2009).

- [32] Luca Salasnich and Boris A. Malomed, Phys. Rev. A **79**, 053620 (2009).
- [33] C.J. Pethick and H. Smith *Bose-Einstein Condensation in Dilute Gases*, 1st ed. (Cambridge University Press, Cambridge, 2002).
- [34] Pere Mujal, Enric Sarlé, Artur Polls, and B Julià-Díaz, Phys. Rev. A **96**, 043614, (2017).
- [35] M. A. H. Ahsan and N. Kumar, Phys. Rev. A **64**, 013608 (2001).
- [36] Mohd Imran and M. A. H. Ahsan Journal of Physics B: Atomic, Molecular and Optical Physics **53**, 125303, (2020).
- [37] Mohd Imran and M. A. H. Ahsan, Adv. Sci. Lett. **21**, 2764-2767, (2015).
- [38] Mohd Imran, M.A.H. Ahsan, Journal of Physics B: Atomic, Molecular and Optical Physics 50 **4**, 045301, (2017).
- [39] Mohd Imran and M. A. H. Ahsan, Communications in Theoretical Physics **65**, 473, (2016).
- [40] Md Hamid, and M. A. H Ahsan, arXiv:2205.11958.
- [41] Mohd. Imran and M. A. H. Ahsan, Eur. Phys. J. D **77**, 79 (2023).
- [42] S. Dutta, Axel U.J. Lode, and Ofir E. Alon, Sci. Rep. **13**, 3343 (2023).
- [43] Mohd Imran and M.A.H. Ahsan, (2017). Novel phases in Bose-Condensed ultra-cold alkali atomic vapours. Jamia Millia Islamia.
- [44] D. G. Fried, T. C. Killian, L. Willmann, D. Landhuis, S. C. Moss, D. Kleppner, and T. J. Greytak, Phys. Rev. Lett. **81**, 3811 (1998).
- [45] I.A. Bhat, T. Mithun, and B. Dey Phys. Rev. E **107**, 044210 (2023).
- [46] N. Barberán, M. Lewenstein, K. Osterloh, and D. Dagnino, Phys. Rev. A **73**, 063623 (2006).
- [47] Pasquale Calabrese, and John Cardy, J. Phys, A: Math. Theor **42** 504005 (2009).
- [48] Tatsuma Nishioka, and Shinsei Ryu, and Tadashi Takayanagi, J. Phys, A: Math. Theor. **42** 504008 (2009).

- [49] R. Horodecki, P. Horodecki, M. Horodecki, and K. Horodecki, *Rev. Mod. Phys.* **81**, 865 (2009).
- [50] Rajibul Islam, Ruicho Ma, Philipp M. Preiss, M. Eric Tai, Alexander Lukin, Matthew Rispoli, and Markus Greiner, *Nature* **528** 77 (2015).
- [51] L. Amico, R. Fazio, A. Osterloh, and V. Vedral, *Rev. Mod. Phys.* **80**, 517 (2008).
- [52] P. Lambropoulos, D. Petrosyans, *Fundamentals of Quantum Optics and Quantum Information* (Springer, Berlin, 2007).
- [53] D. Dagnino, N. Barberán, M. Lewenstein, and J. Dalibard, *Nat. Phys.* **5**, 0431 (2009).
- [54] Jerzy Cioslowski, *J. Phys. B: At. Mol. Opt. Phys.* **50** 235102 (2017).
- [55] Chien-Nan Liu, Akiyoshi Hishikawa, and Toru Morishita, *Phys. Rev. A* **86**, 053426 (2012).
- [56] F. Cajiao Vélez, Lei Geng, J. Z. Kamiński, Liang-You Peng, and K. Krajewska, *Phys. Rev. A* **102**, 043102 (2020).
- [57] F. Dalfovo and S. Stringari, *Phys. Rev. A* **53**, 2477 (1996).
- [58] G. Baym and C.J. Pethick, *Phys. Rev. Lett.*, **76**, 6 (1996).
- [59] Xia-Ji Liu, Hui Hu, Lee Chang, and Shi-Qun Li, *Phys. Rev. A* **64**, 035601 (2001).
- [60] Sergej Moroz, and Dam Thanh Son, *Phys. Rev. Lett.* **122**, 235301 (2019).
- [61] Alexander L. Fetter *Phys. Rev. A* **64**, 063608 (2001).
- [62] Leonardo Brito, Alex Andriati, Lauro Tomio, and Arnaldo Gammal, *Phys. Rev. A* **102**, 063330 (2020).
- [63] O. Penrose, *Philos. Mag.* **42**, 1373 (1951).
- [64] L.D. Landau and E.M. Lifshitz, *Statisticheskaya Fizika (Fizmatgiz, Moscow, 1951)*; *Statistical Physics Pergamon, Oxford, 1958*, Chap. 133.
- [65] Erich J. Mueller, Tin-Lun Ho, Masahito Ueda, and Gordon Baym, *Phys. Rev. A* **74**, 033612 (2006).
- [66] O. Penrose and L. Onsager, *Phys. Rev.* **104**, 576 (1956).

- [67] C.J. Pethick and L.P. Pitaevskii, Phys. Rev. A **62**, 033609 (2000).
- [68] C.N. Yang, Rev. Mod. Phys. **34**, 4 (1962).
- [69] Zhao Liu, Hongli Guo, Shu Chen, and Heng Fan, Phys. Rev. A, **80**, 063606 (2009).
- [70] J. Eisert, M. Cramer, and M.B. Plenio, Rev. Mod. Phys. **82**, 277 (2010).
- [71] B Juliä-Diaz, D. Dagnino, K. J. Günter, T. Graß, N. Barber 'an, M. Lewenstein, and J. Dalibard, Phys. Rev. A **84**, 053605 (2011).
- [72] Xia-Ji Liu, Hui Hu, Lee Chang, Weiping Zhang, Shi-Qun Li, and Yu-Zhu Wang, Phys. Rev. Lett. **87**, 030404 (2001).
- [73] Constantine Yannouleas and Uzi Landman, Phys. Rev. Lett. **85**, 1726 (2000).
- [74] H. Saarikoski, S. Reimann, A. Harju, and M. Manninen, Rev. Mod. Phys. **82**, 2785 (2010).
- [75] F. Chevy, K.W. Madison, and J. Dalibard, Phys. Rev. Lett. **85**, 2223 (2000).
- [76] D.A. Butts, and D.S. Rokhsar, Nature, **397**, 327 (1999).
- [77] N.K. Wilkin, and J.M.F. Gunn, Phys. Rev. Lett. **84**, 6 (2000).
- [78] Chuan-Yin Xia, Hua-Bi Zeng, Yu Tian, Chiang-Mei Chen and Jan Zaanen, Phys. Rev. D, **105**, L021901 (2022).
- [79] S.T. Beliaev, J. Exptl. Theoret. Phys.**34**, 433 (1958).

TABLE I. The many-body ground state energy $E_0^{lab}(\sigma)$ in the laboratory frame for $N = 16$ bosons with interaction strength $g_2 = 0.9151$ and interaction range $\sigma = 0.30, 0.50, 0.75$ in the total angular momentum regime $0 \leq L_z \leq 4N$. For stable angular momentum states, the single particle quantum number (n, m^1) corresponding to the largest eigenvalue λ_1 of OPRDM and the critical angular velocity $\{\Omega_{c_i}(\sigma), i = 1, 2, 3, \dots\}$ are given.

L_z^i	(n, m^1)	$E_0^{lab}(\sigma = 0.30)$	$E_0^{lab}(\sigma = 0.50)$	$E_0^{lab}(\sigma = 0.75)$	$\Omega_{c_i}(\sigma = 0.30)$	$\Omega_{c_i}(\sigma = 0.50)$	$\Omega_{c_i}(\sigma = 0.75)$
0	(0,0)	46.86428	46.35902	45.36785	0.0	0.0	0.0
	(2,0)						
16	(1,1)	59.25225	58.90377	58.46294	0.77425	0.78405	0.81844
	(3,1)						
28	(2,2)	70.13310	69.86716	69.55952	0.90674	0.91362	0.92471
	(4,4)						
30	(2,2)	71.99933	71.73464	71.43247			0.93648
	(4,2)						
32	(2,2)	73.83171	73.59262	73.31758	0.92465	0.93136	0.94256
	(4,2)						
36	(3,3)	77.55398	77.34967	77.12801	0.93255	0.93926	0.95262
	(5,3)						
39	(3,3)	80.39032	80.19670	79.98856			0.95352
	(5,3)						
48	(4,4)	88.89032	88.73774	88.60174	0.94469	0.94901	0.95702
	(6,4)						
52	(4,4)	92.79163	92.64065	93.51604	0.97533	0.97573	0.97464
	(6,4)						
60	(5,5)	100.63525	102.50076	100.35792	0.98045	0.98079	0.98220

TABLE II. For $N = 16$ bosons interacting via Gaussian potential in Eq. (4) with interaction strength $g_2 = 0.9151$ and interaction range $\sigma = 0.30$, the stable ground-state angular momentum states and its span over $L_z - \Omega$ stability graph in Fig. 1 as observed in the co-rotating frame.

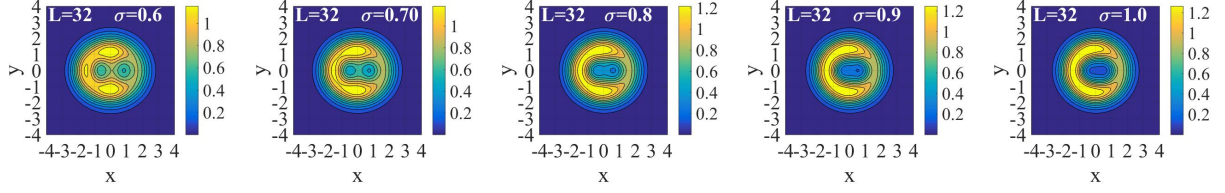
	$L_z(\Omega = 0)$	$L_z(\Omega_{c_1})$	$L_z(\Omega_{c_2})$	$L_z(\Omega_{c_3})$	$L_z(\Omega_{c_4})$	$L_z(\Omega_{c_5})$
Stable vortical states	0	16	28	36	48	60
Angular momentum span	16	12	8	12	12	

TABLE III. For $N = 16$ bosons, values of total angular momentum L_z for which the largest two eigenvalues of OPRDM become comparable *i.e.* $\lambda_2 \approx \lambda_1$ in Fig. 2 for various values of interaction range σ . The interaction strength has been taken $g_2 = 0.9151$ and the total angular momentum in the regime $0 \leq L_z \leq 4N$.

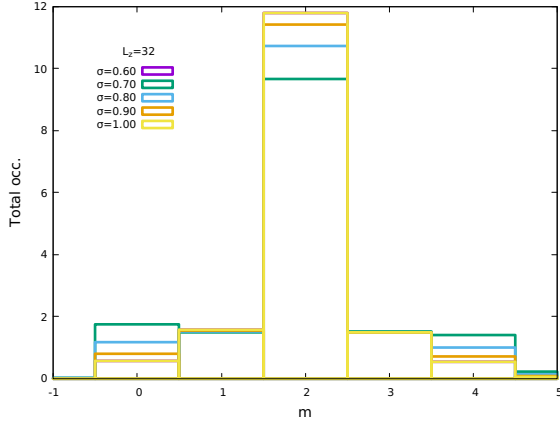
Interaction range σ	Total angular momentum L_z
$\sigma = 0.30$	12 23 34 40 45 50 54 58
$\sigma = 0.50$	12 23 34 40 45 50 54 57 58
$\sigma = 0.75$	12 23 34 35 43 58 62

TABLE IV. For $N = 16$ bosons, values of total angular momentum L_z corresponding to minima in the von Neumann entropy $S_1(L_z, \sigma)$, in Fig. 3, for the interaction strength $g_2 = 0.9151$ and different values of the interaction range σ in Eq. (4) in the total angular momentum regime $0 \leq L_z \leq 4N$. The angular momentum states in bold-face are the stable states, corresponding to plateaus in $L_z - \Omega$ graph in Fig. 1, and other states are the meta-stable states.

Interaction range σ	Total angular momentum L_z
$\sigma = 0.30$	16 19 24 26 28 30 32 36 39 44 48 52 55 60
$\sigma = 0.50$	16 19 24 26 28 30 32 36 39 42 44 48 52 55 60
$\sigma = 0.75$	16 19 24 26 28 30 32 36 39 42 45 48 50 52 55 60



(a) $N = 16$, $L_z = 32$



(b)

FIG. 11. (Color online) The occupation of one-particle angular momentum states of OPRDM *vs* one-particle angular momentum m and the corresponding CPD plots depicting diagonally symmetric two-vortex state with $g_2 = 0.9151$ and $0.6 \leq \sigma \leq 1.0$ in the beyond Lowest-Landau Level approximation. The reference point has been chosen at $\mathbf{r}_0 = (3, 0)$. In CPD plots, yellow represents the highest probability density region and blue the least probability density region as shown on the adjoining color bar: (a) at $L_z = 2N = 32$, with increase in the interaction range beyond $\sigma = 0.7$, the cores begin to merge at $\sigma = 0.80$ and overlap of cores becomes significant. (b) with increase in interaction range σ , the occupation of maximally occupied one-particle angular momentum state $m = 2$ of OPRDM increases.

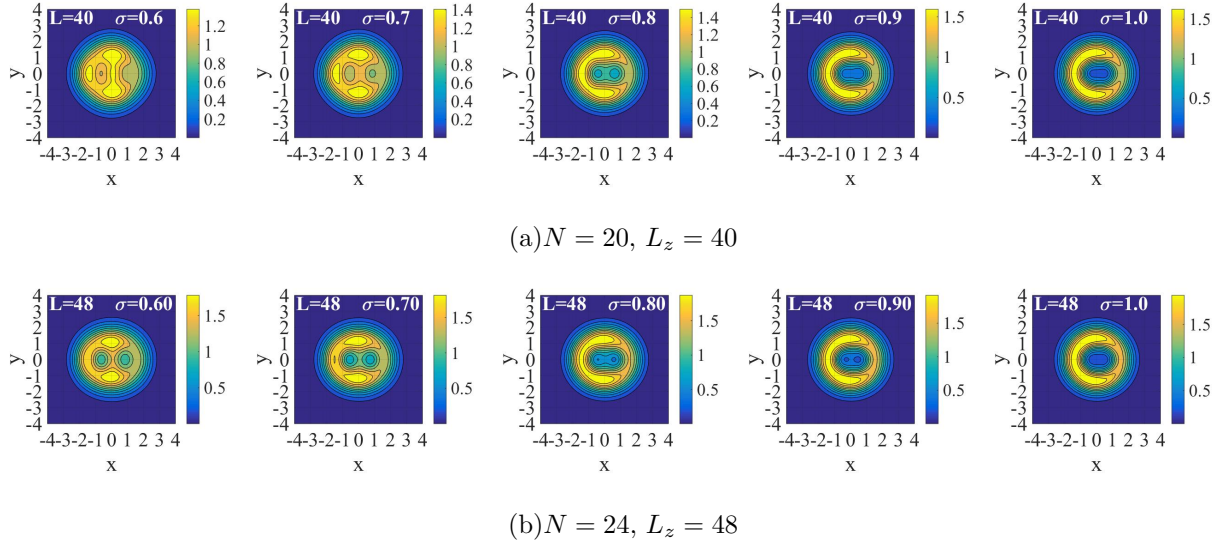
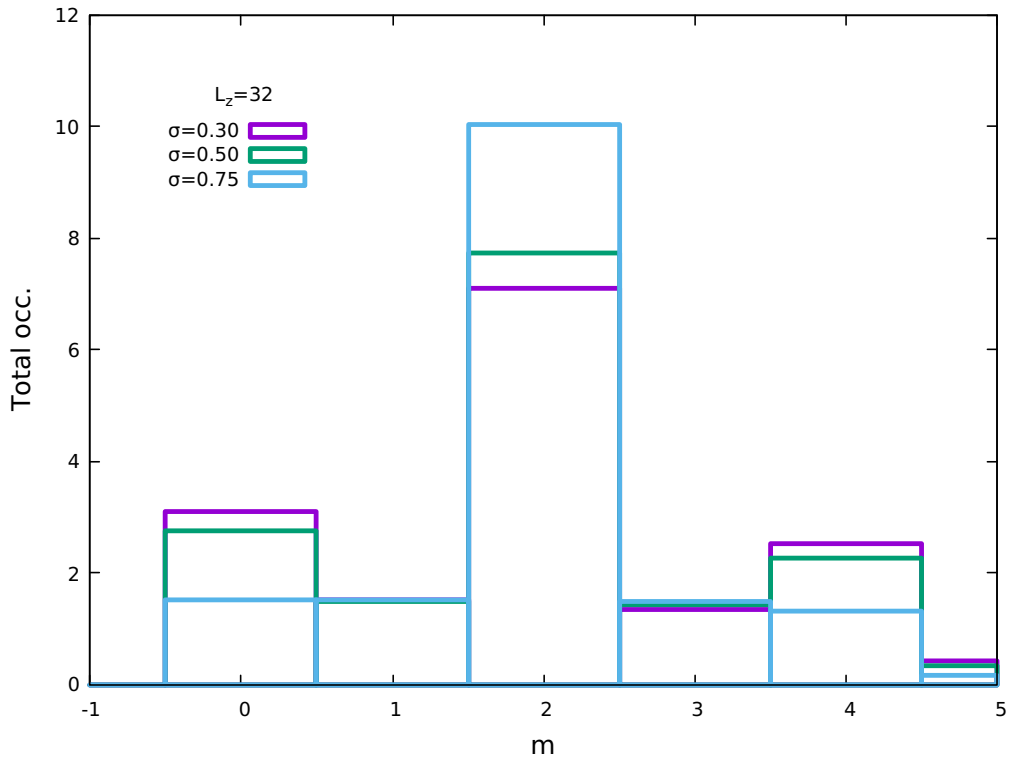
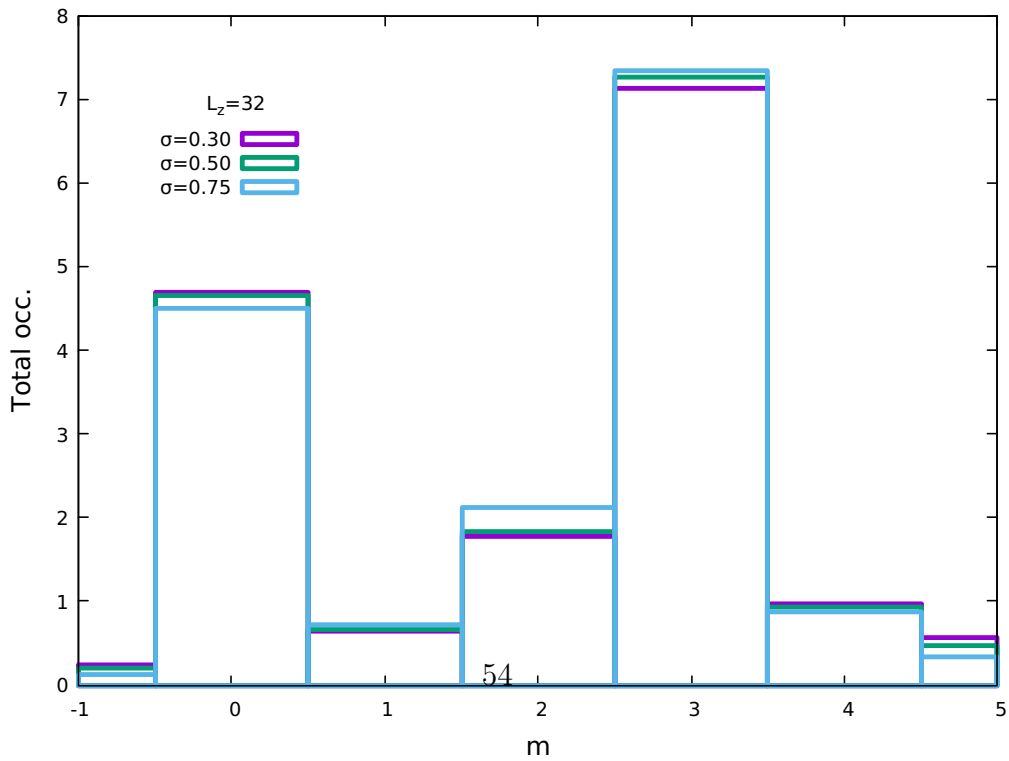


FIG. 12. (Color online) Merging of vortex cores with increase in interaction range: CPD plots depicting diagonally symmetric two-vortex state with $g_2 = 0.9151$ and $\sigma = 0.60 - 1.0$ in the Lowest-Landau Level approximation. The reference point has been chosen at $\mathbf{r}_0 = (3, 0)$. In CPD plots, yellow represents the highest probability density region and blue the least probability density region as shown on the adjoining color bar: (a) at $L_z = 2N = 40$, with increase in interaction range beyond $\sigma = 0.8$, the merging of vortex-cores take place. (b) similarly for $L_z = 2N = 48$ state, with increase in interaction range beyond $\sigma = 0.8$, the vortex cores merge.



(a) $g_2 = 0.09151$



(b) $g_2 = 9.151$

FIG. 13. (Color online) For the angular momentum $L_z = 32$, the occupations of one-particle angular momentum states of OPRDM *vs* one-particle angular momentum states m . (a)

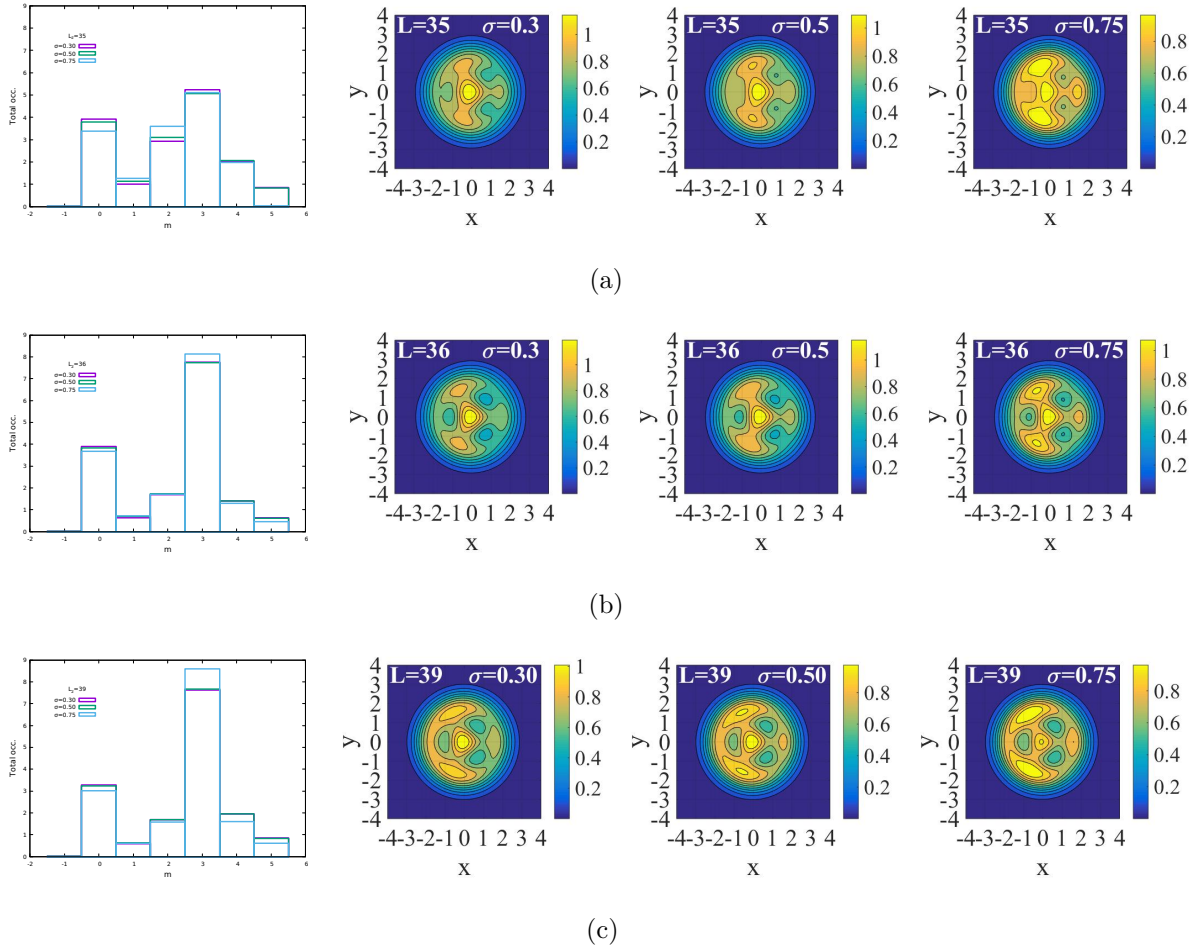


FIG. 14. (Color online) The occupations of one-particle angular momentum states of OPRDM *vs* one-particle angular momentum m and the corresponding CPD plots depicting the three-vortex state for $N = 16$ with interaction strength $g_2 = 0.9151$ and interaction range $\sigma = 0.30, 0.50, 0.75$. The reference point has been chosen at $\mathbf{r}_0 = (1.5, 0)$. In CPD plots, yellow represents the highest probability density region and blue the least probability density region as shown on the adjoining color bar: (a) for the three-vortex meta-stable state $L_z = 35$, with increase in interaction range σ , the occupation of maximally occupied one-particle angular momentum state $m = 3$ of OPRDM decreases whereas, in the CPD plots, the values of probability density at the peaks decrease and at the cores increase. (b) for the three-vortex $L_z = 36$ state, with increase in interaction range σ , the occupation of maximally occupied one-particle angular momentum state $m = 3$ of OPRDM increases whereas, in the CPD plots, the values of probability density at the peaks increases and at the cores decreases, in contrast to $L_z = 35$ state. (c) for the three-vortex $L_z = 39$ state, with increase in interaction range σ , the occupation of maximally occupied one-particle angular momentum state $m = 3$ of OPRDM increases whereas, in the CPD plots, the

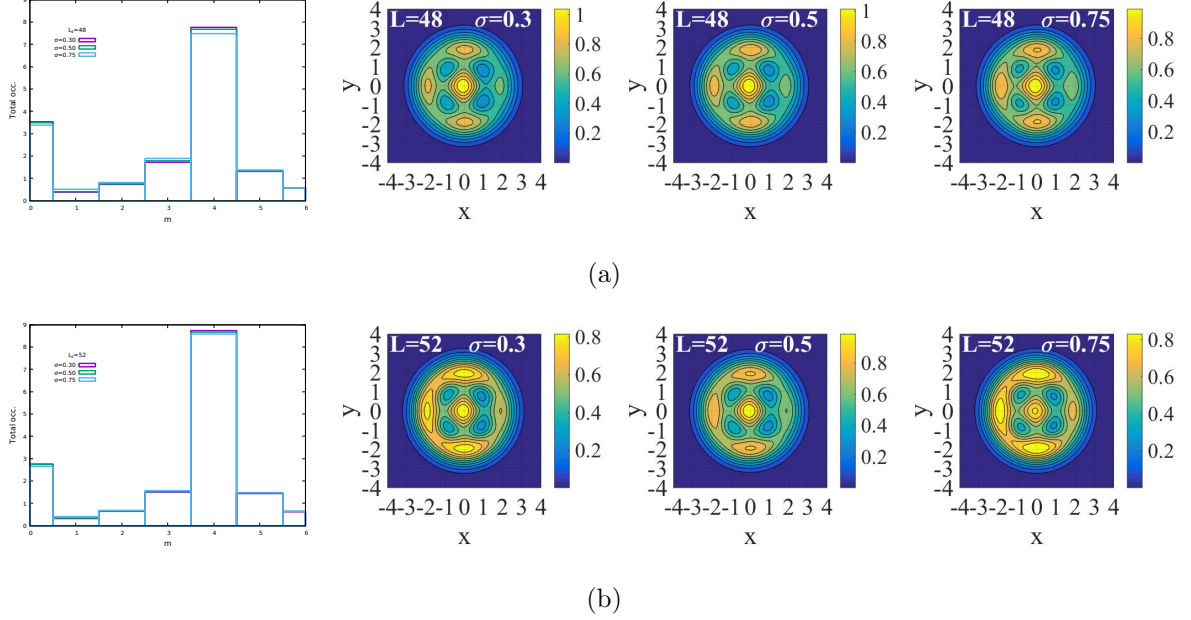


FIG. 15. (Color online) The occupations of one-particle angular momentum state of OPRDM *vs* one-particle angular momentum m and the corresponding CPD plots depicting four-vortex state for $N = 16$ bosons with the interaction strength $g_2 = 0.9151$ and the interaction range $\sigma = 0.30, 0.50, 0.75$. The reference point has been chosen at $\mathbf{r}_0 = (1.5, 0)$. In, yellow represents the highest probability density region and blue the least density region in the adjoining color bar. (a) for $L_z = 48$, with increase in interaction range σ , the occupation of maximally occupied one-particle angular momentum state $m = 4$ of OPRDM decreases whereas, in the CPD plots, the values of probability density at the peaks decrease and at the cores increase. (b) further increase to $L_z = 52$, the occupation of maximally occupied one-particle angular momentum state $m = 4$ of OPRDM increase to the maximum value. With increase in interaction range σ , the occupation of maximally occupied one-particle angular momentum state $m = 4$ of OPRDM does not vary significantly whereas, in the CPD plots, the values of probability density at the peaks increases and at the cores decreases.

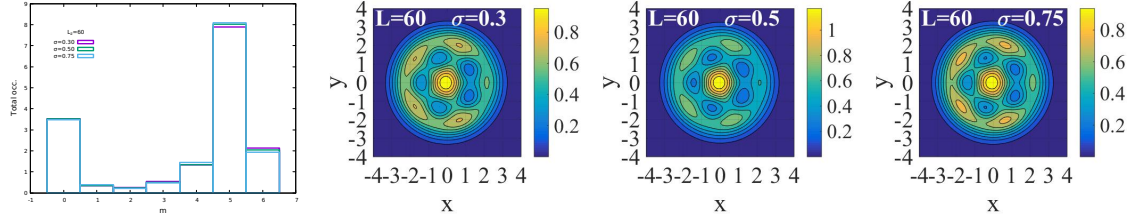


FIG. 16. (Color online) The occupations of one-particle angular momentum state of OPRDM *vs* one-particle angular momentum m and the corresponding CPD plots depicting five-vortex state for $N = 16$ bosons with the interaction strength $g_2 = 0.9151$ and the interaction range $\sigma = 0.30, 0.50, 0.75$. The reference point has been chosen at $\mathbf{r}_0 = (1.5, 0)$. In CPD, yellow represents the highest probability density region and blue the least density region in the adjoining color bar: for $L_z = 60$, with increase in interaction range σ , there is small increase in the occupation of maximally occupied one-particle angular momentum state $m = 4$ of OPRDM, in the CPD plots, the values of probability density at the peaks increases and at the cores decreases.

TABLE V. For $N = 16$ bosons, the largest five eigenvalues $\lambda_1 > \lambda_2 > \lambda_3 > \lambda_4 > \lambda_5$ of OPRDM and the corresponding one-particle basis states (n_μ, m^μ) , $\mu = 1, \dots, 5$ in Eq. (9) for the angular momentum $L_z = 32$ state with interaction strength $g_2 = 0.9151$ and interaction range $\leq \sigma \leq 1$. The largest eigenvalue λ_1 increases with increase in interaction range σ *i.e.* $\lambda_1(\sigma') > \lambda_1(\sigma)$ for $\sigma' > \sigma$.

σ	n_1, m^1	λ_1	n_2, m^2	λ_2	n_3, m^3	λ_3	n_4, m^4	λ_4	n_5, m^5	λ_5
0.00	2,2	0.42220	0,0	0.19470	4,4	0.14026	1,1	0.10217	3,3	0.10028
0.10	2,2	0.42318	0,0	0.19457	4,4	0.14096	1,1	0.10199	3,3	0.09933
0.20	2,2	0.42675	0,0	0.19365	4,4	0.14231	1,1	0.10153	3,3	0.09703
0.30	2,2	0.43495	0,0	0.19058	4,4	0.14261	1,1	0.10069	3,3	0.09468
0.40	2,2	0.45124	0,0	0.18335	4,4	0.13974	1,1	0.09924	3,3	0.09351
0.50	2,2	0.48124	0,0	0.16906	4,4	0.13125	1,1	0.09698	3,3	0.09385
0.60	2,2	0.53230	0,0	0.14395	4,4	0.11418	3,3	0.09455	1,1	0.09435
0.70	2,2	0.60341	0,0	0.10799	3,3	0.09401	1,1	0.09303	4,4	0.08811
0.75	2,2	0.63923	3,3	0.09346	1,1	0.09329	0,0	0.08937	4,4	0.07415
0.80	2,2	0.67015	1,1	0.09402	3,3	0.09303	0,0	0.07299	4,4	0.06163
0.90	2,2	0.71317	1,1	0.09588	3,3	0.09272	0,0	0.04952	4,4	0.04342
1.00	2,2	0.73738	1,1	0.09742	3,3	0.09284	0,0	0.03589	4,4	0.03271

TABLE VI. The three largest eigenvalues $\lambda_1 > \lambda_2 > \lambda_3$ of OPRDM in Eq. (9) for the non-rotating state $L_z = 0$ and the single vortex state $L_z = N$ for $N = 10, 12, 16$ particles with interaction strength $g_2 = 0.9151$ and interaction range $\sigma = 0.30, 0.50, 0.75$.

N	λ_μ $\mu = 1, 2, 3.$	$L_z = 0$			λ_μ $\mu = 1, 2, 3.$	$L_z = N$		
		$\sigma = 0.30$	$\sigma = 0.50$	$\sigma = 0.75$		$\sigma = 0.30$	$\sigma = 0.50$	$\sigma = 0.75$
10	λ_1	0.99240	0.99518	0.99790	λ_1	0.81775	0.82176	0.82451
	λ_2	0.00295	0.00200	0.00094	λ_2	0.09399	0.09210	0.09080
	λ_3	0.00295	0.00200	0.00094	λ_3	0.07767	0.07749	0.07777
12	λ_1	0.99130	0.99436	0.99747	λ_1	0.84247	0.84676	0.84988
	λ_2	0.00329	0.00230	0.00112	λ_2	0.08039	0.07850	0.07716
	λ_3	0.00329	0.00230	0.00112	λ_3	0.06796	0.06753	0.06756
16	λ_1	0.98949	0.99292	0.99664	λ_1	0.87484	0.87949	0.88316
	λ_2	0.00378	0.00278	0.00146	λ_2	0.06268	0.06083	0.05944
	λ_3	0.00378	0.00278	0.00146	λ_3	0.05460	0.05387	0.05355

TABLE VII. The three largest eigenvalues $\lambda_1 > \lambda_2 > \lambda_3$ in Eq. (9) for the ground state of the non-rotating state $L_z = 0$ and the single vortex state $L_z = N$ for $N = 10, 12, 16$ particles with the lesser interaction strength $g_2 = 0.09151$ and the interaction range $\sigma = 0.30, 0.50, 0.75$.

N	λ_μ $\mu = 1, 2, 3.$	$L_z = 0$			λ_μ $\mu = 1, 2, 3.$	$L_z = N$		
		$\sigma = 0.30$	$\sigma = .50$	$\sigma = 0.75$		$\sigma = 0.30$	$\sigma = 0.50$	$\sigma = 0.75$
10	λ_1	0.99990	0.99994	0.99998	λ_1	0.82505	0.82531	0.82541
	λ_2	0.00005	0.00003	0.00001	λ_2	0.09063	0.09047	0.09038
	λ_3	0.00005	0.00003	0.00001	λ_3	0.07829	0.07831	0.07838
12	λ_1	0.99987	0.99993	0.99997	λ_1	0.85078	0.85105	0.85119
	λ_2	0.00005	0.00003	0.00001	λ_2	0.07690	0.07673	0.07663
	λ_3	0.00005	0.00003	0.00001	λ_3	0.06789	0.06789	0.06793
16	λ_1	0.99983	0.99991	0.99996	λ_1	0.88472	0.88500	0.88517
	λ_2	0.00007	0.00004	0.00002	λ_2	0.05899	0.05883	0.05873
	λ_3	0.00007	0.00004	0.00002	λ_3	0.05358	0.05355	0.05357

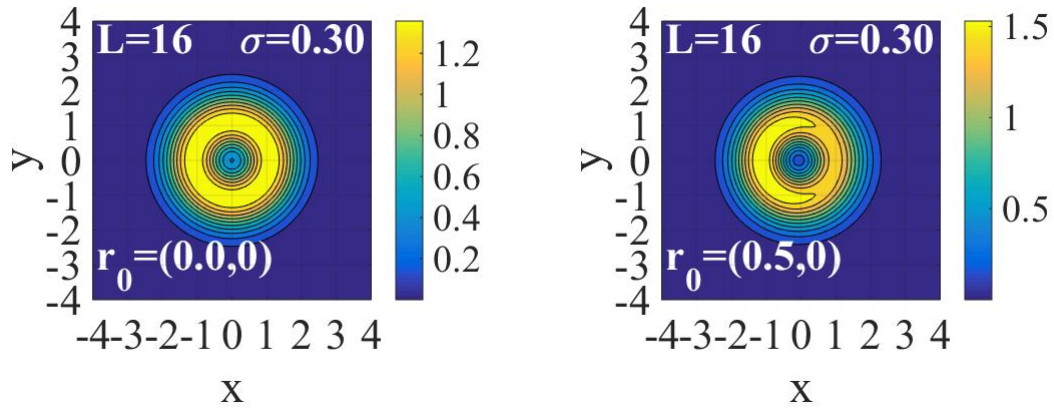


FIG. 17. (Color online) CPD plots depicting single-vortex state for $L_z = N = 16$ bosons with the interaction strength $g_2 = 0.9151$ and the interaction range $\sigma = 0.30$. The CPD exhibits cylindrical symmetry when reference point \mathbf{r}_0 coincides with trap centre, whereas, the cylindrical symmetry is broken as the reference point is moved from the trap centre. In the color bar, yellow represents the highest probability density region and blue the least density region.